Atmos. Chem. Phys., 13, 10827–10845, 2013
www.atmos-chem-phys.net/13/10827/2013/
doi:10.5194/acp-13-10827-2013

Atmospheric Chemistry and Physics Open Access

Spatial distribution of dust's optical properties over the Sahara and Asia inferred from Moderate Resolution Imaging Spectroradiometer

M. Yoshida[1,2], **J. M. Haywood**[3,4], **T. Yokohata**[5], **H. Murakami**[6], **and T. Nakajimae**[1]

[1]Atmosphere and Ocean Research Institute, University of Tokyo, Chiba, Japan
[2]Remote Sensing Technology Center of Japan, Tsukuba, Japan
[3]Met Office Observation Based Research, Exeter, UK
[4]College of Engineering, Mathematics and Physical Sciences, University of Exeter, Exeter, UK
[5]National Institute for Environmental Studies, Tsukuba, Japan
[6]Japan Aerospace Exploration Agency, Tsukuba, Japan

Correspondence to: M. Yoshida (mayum@restec.or.jp)

Received: 17 September 2012 – Published in Atmos. Chem. Phys. Discuss.: 5 December 2012
Revised: 12 July 2013 – Accepted: 11 September 2013 – Published: 7 November 2013

Abstract. There is great uncertainty regarding the role of mineral dust aerosols in Earth's climate system. One reason for this uncertainty is that the optical properties of mineral dust, such as its single scattering albedo (the ratio of scattering to total extinction), are poorly constrained because ground observations are limited to a few locations and satellite standard products are not available due to the excessively bright surface of the desert in the visible wavelength, which makes robust retrievals difficult. Here, we develop a method to estimate the spatial distributions of the aerosol single scattering albedo (ω_0) and optical depth (τ_a), with daily $1^\circ \times 1^\circ$ spatial resolution using data from the Moderate Resolution Imaging Spectroradiometer (MODIS) as well as model simulations of radiative transfer. This approach is based on the "critical surface reflectance" method developed in the literature, which estimates ω_0 from the top of the atmospheric radiance. We estimate the uncertainties in ω_0 over the Sahara (Asia) to be approximately 0.020 and 0.010 (0.023 and 0.017) for bands 9 and 1, respectively, while the uncertainty in τ_a is approximately 0.235 and 0.228 (0.464 and 0.370) for bands 9 and 1, respectively. The 5–95 % range of the spatial distribution of ω_0 over the Sahara (Asia) is approximately 0.90–0.94 and 0.96–0.99 (0.87–0.94 and 0.89–0.97) for bands 9 and 1, respectively, and that of τ_a over the Sahara (Asia) is approximately 0.8–1.4 and 0.8–1.7 (0.7–2.0 and 0.7–1.9) for bands 9 and 1, respectively. The results for the Sahara indicate a good correlation between ω_0 and the surface reflectance, and between ω_0 and τ_a. However, the relationships between ω_0, τ_a, and surface reflectance are less clear in Asia than in the Sahara, and the ω_0 values are smaller than those in the Sahara. The regions with small ω_0 values are consistent with the regions where coal-burning smoke and carbonaceous aerosols are reported to be transported in previous studies. Because the coal-burning and carbonaceous aerosols are known to be more absorptive and have smaller ω_0 values than dust aerosols, our results indicate that the dust aerosols in Asia are contaminated by these anthropogenic aerosols. The spatial distribution of dust optical properties obtained in our work could be useful in understanding the role of dust aerosols in Earth's climate system, most likely through future collaboration with regional and global modelling studies.

1 Introduction

Aerosols are one of the most uncertain factors in determining the energy budget of the earth's climate system. Species of aerosols with significant radiative forcing include sulphates, fossil fuel organics, black carbon, biomass burning, nitrates, and mineral dust (Forster et al., 2007). Among these species, mineral dust can both scatter and absorb solar radiation and

absorb and emit terrestrial radiation (e.g., Andreae, 1995). Measurements of mineral dust's direct radiative effect (DRE) over the ocean have suggested that local DRE could be extremely strong (Forster et al., 2007). The global DRE of mineral dust based on recent model simulations ranges from -0.56 to $+0.1\,\mathrm{W\,m^{-2}}$, indicating major uncertainty regarding the role of mineral dust in the climate system (Forster et al., 2007).

One reason for this uncertainty about the radiative effect of mineral dust is that mineral dust's optical properties are poorly understood and poorly characterised (e.g., Sokolik et al., 2001). Among dust optical parameters, the single scattering albedo (the ratio of scattering to total extinction cross sections) is particularly important for quantifying radiative forcing. For example, Hansen et al. (1997) found that the critical single scattering albedo at which the aerosol's impact on the global mean surface temperature shifted from cooling to heating was approximately 0.91 in the visible spectrum when "semidirect" aerosol effects were included (i.e., that aerosol absorption causes a positive climate feedback by reducing local large-scale cloud cover).

The World Meteorological Organisation (WMO) recommended an imaginary refractive index of 0.008, corresponding to dust's single scattering albedo (ω_0) of 0.653 at 0.55 µm (WMO, 1983). However, observations from the ground and from aircraft over the Sahara suggest significantly smaller dust absorption values than those given by the WMO. Haywood et al. (2003) reported values of 0.95–0.99 from the Saharan Dust Experiment (SHADE, Tanré et al., 2003), and McConnell et al. (2008) reported a range of 0.95–0.99 during the Dust Outflow and Deposition to the Ocean (DODO, McConnell et al., 2008) experiment. Osborne et al. (2008) estimated the ω_0 for pure dust aerosol during the Dust and Biomass-burning Experiment (DABEX, Haywood et al., 2008) to be consistently high, within a range of 0.98–0.99. According to Johnson and Osborne (2011), ω_0 values at 0.55 µm were measured within the range of 0.92–0.99 during the Geostationary Earth Radiation Budget Intercomparison of Long-wave and Short-wave (GERBILS) radiation (Haywood et al., 2011) campaign. More recently, ω_0 was measured very close to fresh dust sources during the Fennec program, and the 0.55 µm values ranged from 0.7 to 0.97, due to the presence of a significant number of large particles (Ryder et al., 2013). Analyses of the ω_0 values of Saharan dust from the Aerosol Robotic Network (AERONET, Holben et al., 1998) suggested an average of 0.95 at 0.67 µm (Dubovik et al., 2002).

Ground observations of ω_0 were also performed over the Asian region. Unpolluted Asian dust analysed during the Aeolian Dust Experiment on Climate (ADEC, Mikami et al., 2006) had an average ω_0 of 0.93 at 0.67 µm, and ω_0 values of 0.90 and 0.89 were obtained from ground-based radiation measurements (Kim et al., 2004, 2005). Based on observations at the dust source and surrounding regions, dust over Asia was reported to mix with soot particles produced over industrial areas, leading to stronger absorption and a reduced ω_0 (Kim et al., 2004, 2005; Sohn et al., 2007).

In addition to these ground observations, optical properties of dust have been estimated from satellite observations. While satellite data can, in the absence of clouds, provide continuous observations over large areas with low reflectance, it is not easy to provide aerosol properties over an entire desert area because the desert's surface is too bright in the visible wavelengths. Kaufman et al. (2001) estimated the ω_0 over the Sahara using the "critical surface reflectance" method, which requires information on aerosol optical depth (τ_a), but their analysis was limited to a particular location over the Sahara because they had to use a τ_a value derived from independent ground measurements. The Deep Blue algorithm (Hsu et al., 2004) retrieved aerosol properties from satellite data over bright surfaces such as arid and semiarid areas, but the ω_0 was only estimated at wavelengths below 500 nm by assuming that it was constant at 670 nm. More recently, Zhu et al. (2011) estimated the spatial distribution of absorption by aerosols produced during biomass burning using the critical surface reflectance method described above, but their method cannot be applied to desert areas because information on τ_a values is not available for such areas.

In summary, studies of the optical properties of dust obtained over desert areas have been limited to certain locations due to the difficulty of performing ground and satellite observations. Therefore, the spatial and temporal distributions of dust's optical properties have not yet been extensively estimated. The chemical properties of mineral dust at Earth's surface vary over space and time, and dust aerosols can be mixed with other aerosols during transportation. Therefore, the spatial and temporal distributions of dust's optical properties may affect the climate states over and around desert areas. The impact of geographical variations in chemical composition and hence in optical properties has not yet been considered in global or regional models (Forster et al., 2007).

In the present study, we investigate the spatial distribution of dust optical properties (such as ω_0 and τ_a) over desert areas using nine years of data from the Moderate Resolution Imaging Spectroradiometer (MODIS) on board the Aqua satellite. Special attention is given to the optical properties of dust over the Saharan and Asian desert regions. The general features of the dust aerosol's optical properties are discussed by comparing the optical properties of these different regions.

Our methodology is based on the theory that the critical surface reflectance, the observed radiance of which is uninfluenced by the variability in dust's optical depth, depends on ω_0 (Kaufman, 1987; Kaufman et al., 2001). Yoshida and Murakami (2008) also used the critical surface reflectance method and investigated the mean value of ω_0 over the Saharan region using long-term MODIS satellite data. We extend the approach of Yoshida and Murakami (2008) and explore the spatial distribution of ω_0 and τ_a at resolutions of 1° longitude and 1° latitude using daily MODIS data. The details of our methodology are explained in Sect. 2, and Sect. 3

gives the optical properties of the dust that we estimated over the Sahara and Asia. Finally, our results are summarised in Sect. 4.

2 Methodology

We estimate the single scattering albedo and optical depth of dust using MODIS satellite data and model simulations based on the method developed by Kaufman (1987) and Kaufman et al. (2001). The basic concept of our methodology is given in Sect. 2.1. Descriptions of the MODIS satellite data and radiative transfer model simulations are given in Sects. 2.2 and 2.3, respectively. Details on the procedure for retrieving τ_a and ω_0 are given in Sect. 2.4.

2.1 Basic concept

The basic concept of our methodology is illustrated in Fig. 1. The reflectance at the top of the atmosphere (TOA) is simulated using the radiative transfer model described in Sect. 2.3 under hazy and clear conditions (the definition of hazy and clear conditions is given in Sect. 2.4). Figure 1 shows the difference between the TOA reflectances in hazy and clear conditions ($\Delta\rho^t$) as a function of the TOA reflectance in clear conditions (ρ^t_{clear}), using the radiative transfer model by changing the surface reflectance from 0.0 to 0.6 in the simulation. The single scattering albedo (ω_0) and optical depth (τ_a) of dust are perturbed in Fig. 1. The results for $\omega_0 = 0.970$ (dashed) and 0.901 (solid) and $\tau_a = 1.0$ (blue), 2.0 (green), and 3.0 (red) are shown in Fig. 1.

Figure 1 shows that for dark surfaces (small ρ^t_{clear} in Fig. 1) the TOA reflectance increases as the dust's optical depth increases, whereas for bright surfaces (large ρ^t_{clear} in Fig. 1) the TOA reflectance decreases as the dust's optical depth increases. As shown in Fig. 1, the critical surface reflectance (ρ_c), for which the TOA reflectance (critical TOA reflectance ρ^t_c) is uninfluenced by the variability in the dust's optical depth, depends on ω_0. At ρ_c, there is a balance between the brightening of the surface by atmospheric scattering and the darkening of the surface by aerosol absorption (Kaufman, 1987; Haywood and Shine, 1995). ρ_c and ρ^t_c can be obtained by satellite observation; thus, we can estimate the ω_0 of the dust based on the radiative transfer model simulations.

In Kaufman (1987) and Kaufman et al. (2001), the τ_a values are based on independent ground measurements. In general, the number of ground measurements in the desert regions was very small, and τ_a was not estimated over desert areas in the standard satellite products of the visible wavelengths because the surface albedo of the desert was too high. In this study, τ_a is estimated along with ω_0, making our method advantageous compared with previous studies because we can estimate τ_a and ω_0 simultaneously whenever the appropriate satellite data are available, thus providing far greater spatial coverage.

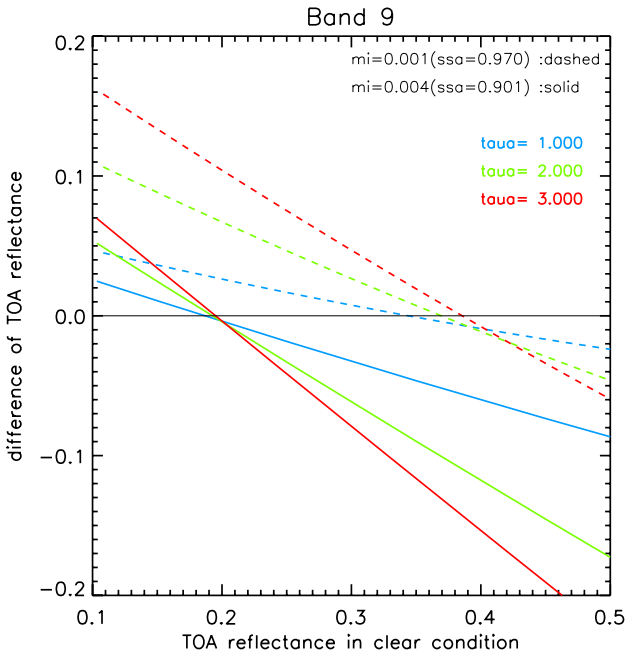

Fig. 1. A sample radiative transfer model simulation illustrating the essence of the "critical surface reflectance" method developed by Kaufman (1987). The horizontal axis is the top-of-the-atmosphere (TOA) reflectance in clear conditions (ρ^t_{clear}), and the vertical axis is the difference between TOA reflectance during hazy and clear conditions (ρ^t-$\rho^t_{clear} = \Delta\rho^t$). The lines in the diagram are calculated by changing the surface reflectance from 0.0 to 0.6 (intervals of 0.01) in the model simulations. The dust optical parameters, such as the single scattering albedo (ω_0) and optical depth (τ_a), are perturbed in the model simulations. The dashed line represents the simulation with $\omega_0 = 0.970$ (ω_0 is perturbed through the imaginary refractive index, m_i, and in this case $m_i = 0.001$), and the solid line is that with $\omega_0 = 0.901$ ($m_i = 0.004$). The optical depths of the dust aerosols used in the simulations are 1.0 (blue), 2.0 (green), and 3.0 (red). The simulations are performed at a solar zenith angle of 10°, a satellite zenith angle of 30°, and a relative azimuth angle of 180°, and the wavelength is 0.443 µm. The model parameters related to the dust aerosols are given by the mean values in Table 1.

The method we devised in this study is as follows. As illustrated in Fig. 1, the slope of the $\rho^t - \rho^t_{clear}(\Delta\rho^t)$ versus ρ^t_{clear} diagram depends on τ_a: the absolute value of the slope is greater for larger τ_a values because, if the dust aerosol is thick enough (i.e., τ_a is large), when we change the surface albedo, the difference in the TOA reflectance between hazy and clear skies ($\Delta\rho^t$) changes accordingly. We estimate the τ_a and ω_0 values based on the fact that the features of the ρ^t_{clear} versus $\Delta\rho^t$ diagram are dependent on τ_a and ω_0. The relationship between the slope of the ρ^t_{clear} versus $\Delta\rho^t$ diagram (α) and τ_a is derived in the Appendix. While the methodological concepts are explained using approximation theory in the Appendix, the computations in Sects. 2 and 3 are performed using a rigorous radiative transfer as described in Sect. 2.3. The ρ^t_{clear} versus $\Delta\rho^t$ diagram is created using

Table 1. Mean values and standard deviations of the aerosol model parameters calculated from AERONET data.

Model parameters		Sahara		Asia	
		Mean	Standard deviation	Mean	Standard deviation
Volume median radius [μm]	Fine mode ($r_{v,1}$)	0.183	0.040	0.155	0.034
	Coarse mode ($r_{v,2}$)	2.127	0.309	2.355	0.450
Standard deviation	Fine mode (σ_1)	1.865	–	1.751	–
	Coarse mode (σ_2)	1.785	–	1.845	–
Particle volume concentration [$\mu m^3/\mu m^2$]	Fine mode ($C_{v,1}$)	0.026	0.011	0.062	0.055
	Coarse mode ($C_{v,2}$)	0.385	0.240	0.486	0.431
Real part of the refractive index	Band 9 (m_r)	1.497	0.045	1.523	0.062
	Band 1 (m_r)	1.508	0.038	1.534	0.051
Aerosol optical depth for clear conditions	Band 9 (τ_{a_clear})	0.254	0.114	0.241	0.126
	Band 1 (τ_{a_clear})	0.212	0.116	0.196	0.134

the daily $1^\circ \times 1^\circ$ latitude-longitude data from the MODIS satellite, allowing us to estimate τ_a and ω_0 at these space and time resolutions. The estimated τ_a and ω_0 can be considered the average of a $1^\circ \times 1^\circ$ grid. We also evaluate the uncertainties of our estimation in Sect. 3.1.

2.2 Satellite data

We use Level-1B radiance data sub-sampled at 5 km by MODIS on board the NASA EOS Aqua spacecraft (http://modis.gsfc.nasa.gov/). The MODIS data for bands 9 (0.438–0.448 μm) and 1 (0.620–0.670 μm) are used for this analysis because bands 1 and 9 are the bands at which the optical properties of AERONET ground observations are available (Holben et al., 1998). The target area for the analysis is the land area from 10° to 35° north and 20° west to 30° east over the Sahara and from 34° to 45° north and 75° to 145° east over Asia. We use nine years of data (from 2003 to 2011 and select May–August in the Sahara and March–May in Asia because dust events often occur during these months in each region. Additionally, peak biomass burning emissions from the Sahel that are advected over the Sahara in December–February are avoided (Haywood et al., 2008, 2011). To select clear-sky (i.e., cloud-free) conditions, we use the cloud mask from Level-2 MODIS atmosphere products (Ackerman et al., 1998). To distinguish between clear and hazy conditions, we use the aerosol index values (Herman et al., 1997; Torres et al., 1998) from the Earth Probe's Total Ozone Mapping Spectrometer (TOMS) for 2003–2005 and those from an Ozone Monitoring Instrument (OMI) for 2006–2011 (Torres et al., 2002, 2007).

2.3 Simulations with a radiative transfer model

We use a radiative transfer code called System for the Transfer of Atmospheric Radiation developed at the University of Tokyo (RSTAR, Nakajima and Tanaka, 1986, 1988; Stamnes et al., 1988) for the model simulations. Because many studies indicate that a bimodal lognormal function is the most appropriate model for aerosol particle size distribution (cf. Whitby, 1978; Shettle and Fenn, 1979; Remer and Kaufman, 1998), we use the following dust size (r_d) distribution:

$$\frac{dV(r_d)}{d\ln r_d} = \sum_{i=1}^{2} \frac{C_{v,i}}{\sqrt{2\pi}\ln\sigma_i} \exp\left[-\frac{(\ln r_d - \ln r_{v,i})^2}{2\ln^2\sigma_i}\right], \quad (1)$$

where index i denotes the fine ($i = 1$) and coarse ($i = 2$) modes of the aerosol, $C_{v,i}$ is the particle volume concentration, $r_{v,i}$ is the volume median radius, and σ_i is the standard deviation. For the shape of the aerosol, we assume a non-spherical yellow dust model (Nakajima et al., 1989), employing the non-spherical parameters from a semi-empirical theory by Pollack and Cuzzi (1980) with an r of 1.1, an $X0$ of 7, and a G of 10.

The aerosol size distribution parameters ($C_{v,1}$, $r_{v,1}$, σ_1, $C_{v,2}$, $r_{v,2}$, σ_2) and the real part of the refractive index (m_r) in the model simulation are derived from AERONET Level 2.0 inversion data (Dubovik and King, 2000, http://aeronet.gsfc.nasa.gov) for hazy conditions. Non-spherical aerosol is assumed in the inversion of the AERONET data (Dubovik et al., 2006). The aerosol's optical depth for clear conditions (τ_{a_clear}) is also derived from AERONET Level 2.0 direct sun algorithm data (O'Neill et al., 2003) in clear conditions. These values are distinguished as hazy conditions (aerosol index greater than 3) and clear conditions (aerosol index less than or equal to 2) using the corresponding TOMS or OMI data. Here, we use the TOMS and OMI data for the classification of clear and hazy conditions because of the consistency with the classification of MODIS satellite data used for the analysis, as described in Sect. 2.4.

The values of the model parameters are shown as the mean listed in Table 1. Here, $C_{v,1}$ and $C_{v,2}$ are used to determine the ratio of volume concentration between the fine and the coarse mode, and the aerosol's total column density is determined by the aerosol's optical depth. In the present study, uncertainties of the model parameters are considered using the standard deviation listed in Table 1. The mean and standard deviation values in Table 1 are derived from the AERONET

data using the observational sites shown in Fig. 4 for the Sahara and Fig. 9 for Asia. The uncertainties in the model simulations concerning the estimation of τ_a and ω_0 are described in Sect. 3.1.

In the radiative transfer simulations, we consider the altitude of the surface over the Sahara and Asia using the ETOPO1 global relief model (Amante and Eakins, 2009). Original ETOPO1 data with a 1 min spatial resolution are averaged to a 1° resolution for the calculation.

2.4 Procedure for estimating τ_a and ω_0

This section describes the procedures used to estimate τ_a and ω_0. First, we sample the TOA reflectance from the daily MODIS satellite data in clear and hazy conditions with various surface reflectances within 1° longitude and 1° latitude. We then create a scatter plot of the ρ^t_{clear} versus $\Delta\rho^t$ diagram and derive the critical TOA reflectance (ρ^t_c) and slope of the diagram (α), as illustrated in Fig. 2. The points in Fig. 2 are obtained from 0.05° × 0.05° MODIS satellite data within the 1° × 1° grid (thus, the maximin number of points is 400). Because the surface reflectance varies spatially, we can obtain the scatter plot shown in Fig. 2 with the daily 1° × 1° resolution.

For clear conditions, we use the inclusion criterion that the aerosol index obtained from TOMS or OMI on the same day be less than or equal to 2. ρ^t_{clear} is derived from the time average of TOA reflectance during clear conditions. The time average is derived from data for every 16 days (the MODIS recurrence period) due to the surface's bidirectional characteristics and the differences in atmospheric path length and scattering phase function. Therefore, we have 16 different ρ^t_{clear} values according to the MODIS geometry.

For hazy conditions, we consider the criterion that the aerosol index is greater than 3. We chose a threshold value of 3 because it is the value at which we can obtain a sufficient difference between ρ^t and ρ^t_{clear} and because it provides a sufficient number of data points for the analysis. We evaluate the average of the AERONET data and find that aerosol indexes 2 and 3 correspond to aerosol optical depths of 0.39 and 0.57, respectively, at 0.440 µm. Here, we choose the 0.05° × 0.05° data with a MODIS cloud mask to be "confidently clear" in the selection of both clear and hazy conditions. For the calculation of $\Delta\rho^t = \rho^t - \rho^t_{clear}$, we use a ρ^t_{clear} value with a sensor zenith angle identical to that of the ρ^t during hazy conditions.

From the scatter plot in the ρ^t_{clear} versus $\Delta\rho^t$ diagram, we derive the critical TOA reflectance (ρ^t_c) and slope (α). In this method, it is important to have a reasonable spread in ρ^t_{clear} in order to make reliable estimations of ρ^t_c and α. Therefore, we do not include grids with homogeneous surface reflectance; thus, the spread in ρ^t_{clear} is very small. For this purpose, we divide ρ^t_{clear} into bins with 0.05 widths, and we select grids whose data span more than 5 bins (the number of data in each bin is more than 7). Then, both ρ^t_c and α are estimated only

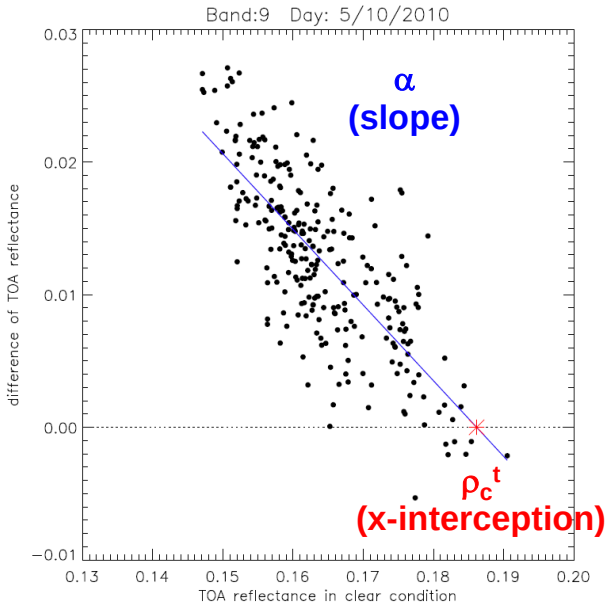

Fig. 2. This figure is identical to Fig. 1 but is created from the MODIS satellite data. Each dot is calculated from TOA reflectances on 10 May 2010 with 0.05° × 0.05° data. The mean observed geometry is a solar zenith angle of 17.1°, a satellite zenith angle of 42.4°, and a relative azimuth angle of 159.8°, and the wavelength is 0.443 µm. This diagram is created using daily TOA reflectance data within a 1° × 1° grid box, and thus, the maximum number of points in a diagram is 400. The fitted line (blue) is calculated with the least-squares method, after which the x intercept (critical TOA reflectance ρ^t_c) and slope (α) are estimated. From the look-up table for the relationship between [ρ^t_c, α] and [single scattering albedo (ω_0), optical depth (τ_a)] as shown in Fig. 3, the ω_0 and τ_a values are estimated from the daily 1° × 1° resolution.

when they are statistically significant using the least-squares method. The results are deemed statistically significant when the null hypothesis (population regression coefficient $\alpha = 0$) is rejected with a significance level of 0.05. The test of null hypothesis $\alpha = 0$ is performed under the assumption that the F statistic described below follows an F distribution with (k, $n-k-1$) degrees of freedom:

$$F = \frac{\frac{S_R}{k}}{\frac{S_E}{n-k-1}} = \frac{\frac{R^2}{k}}{\frac{1-R^2}{n-k-1}}, \quad (2)$$

where S_R is the square sum of the regression, S_E is the square sum of errors, R is the multiple correlation coefficient, and n and k are the number of data points and explanatory variables, respectively. Using this statistical test, we can reject the case where the spread in the scatter plot is too large, with the result that ρ^t_c (x intercept) and α (slope) are not properly estimated. Although the regression line is deemed statistically significant, the spread in the scatter plot causes uncertainties in the estimation of ρ^t_c and α, which yields uncertainties in the estimation of aerosol optical properties (τ_a and

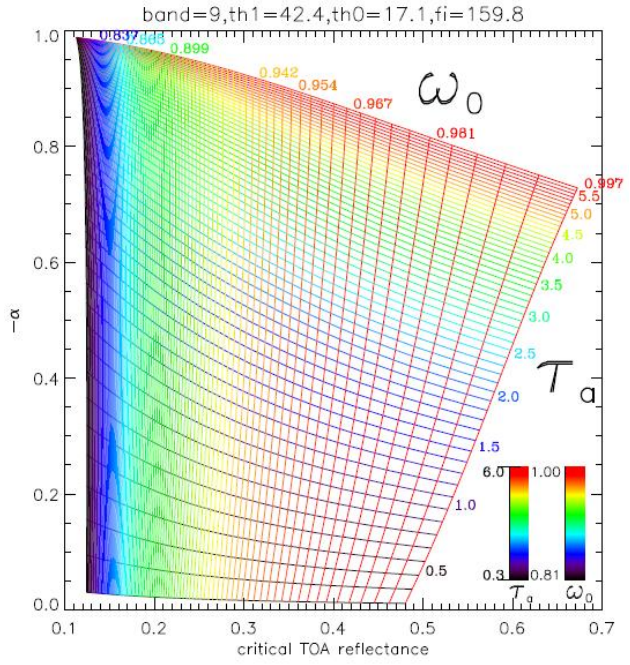

Fig. 3. An example of a look-up table (LUT) calculated from the radiative transfer model simulations. The LUT is used to estimate the dust's single scattering albedo (ω_0) and optical depth (τ_a) from the values of the x intercept (critical TOA reflectance ρ_c^t) and the slope (α) as defined in Fig. 2. Here, we give 100 different ω_0 values (through perturbing the imaginary part of the refractive index) and 57 different τ_a values in the model simulation. We then calculate the ρ_c^t and α values as demonstrated in Fig. 1. The satellite and solar geometry, the aerosol model parameters, and the wavelength are the same as those in Fig. 2.

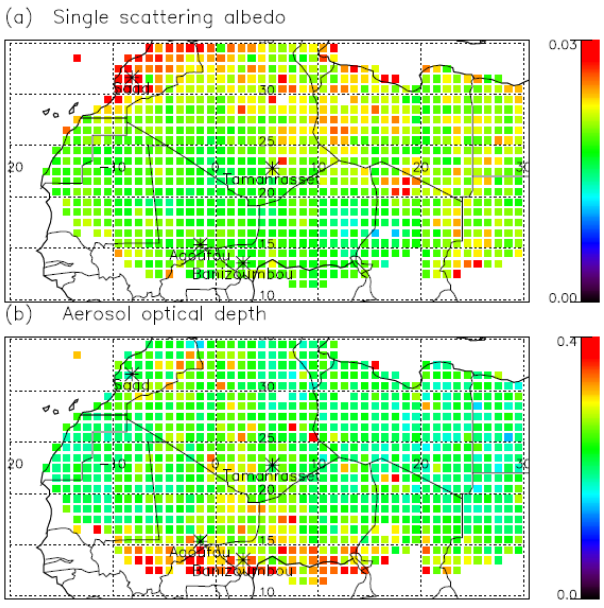

Fig. 4. Spatial distribution of the total uncertainties in band 9 for the estimation of **(a)** the single scattering albedo ω_0 and **(b)** the optical depth τ_a over the Sahara. The AERONET sites of Agoufou, Banizoumbou, Saada, and Tamanrasset are also shown.

ω_0). The uncertainties in τ_a and ω_0 are evaluated in Sect. 3.2 (Tables 2 and 3). To connect the values of [ρ_c^t, α] obtained from the scatter plot to the [ω_0, τ_a] values, we perform the model simulations described in Sect. 2.3 in advance and create the look-up tables (LUTs) shown in Fig. 3. To calculate the LUTs, we calculate $\Delta\rho^t$ and ρ_{clear}^t by perturbing the surface reflectance and then calculate [ρ_c^t, α] from the ρ_{clear}^t versus $\Delta\rho^t$ diagram. In the LUT calculation, we use the two wavelengths corresponding to bands 1 and 9 with various geometries (solar and satellite zenith angles and the azimuth angle between the sun and satellite).

When the surface reflectance is low enough and there are no data with $\Delta\rho^t = 0$ (and thus ρ_c^t), the regression line of the scatter plot is extrapolated to find ρ_c^t, where $\Delta\rho^t = 0$. As shown in Fig. 1, the relationship between ρ_{clear}^t and $\Delta\rho^t$ is nearly linear, but it includes non-linear components. Therefore, we create four different LUTs for four different ρ_{clear}^t ranges (ρ_{clear}^t of <0.15, 0.15–0.20, 0.20–0.25, >0.25 at band 9, and ρ_{clear}^t of <0.20, 0.20–0.30, 0.30–0.40, >0.40 at band 1).

In the present study, the aerosol's optical properties, estimated as described above, are compared with the ground observations in Sect. 3.2. For the Sahara, the AERONET data (site locations indicated in Fig. 4) are used for the validation. For Asia, the observational data from the Skyradiometer Network (SKYNET, http://atmos.cr.chiba-u.ac.jp/) are used (site locations shown in Fig. 9).

3 Results and discussion

Uncertainties in our estimation are investigated in Sect. 3.1. In Sect. 3.2 we then evaluate our method by comparing the dust properties we estimated with ground observations. The results of the spatial distribution of aerosol optical properties over the Sahara and Asia are presented in Sect. 3.3. The reasons for the difference between the two regions' optical properties are discussed in Sect. 3.4.

3.1 Uncertainties in the estimation of dust's optical properties

This section examines the uncertainties in our estimation of dust's ω_0 and τ_a values. There are eleven possible reasons for the uncertainties in our method, and they can be classified into two types: uncertainties related to the observations (1 to 7 described below) and uncertainties related to the model simulations (8 to 11). The uncertainty from each component and the total uncertainty over the Sahara and Asia are summarised in Tables 2 and 3, respectively.

Table 2. Uncertainties in ω_0 and τ_a due to error sources shown from (1) to (11) for bands 9 and 1 over the Sahara. The total uncertainties are shown in the rightmost column. The uncertainties related to the observations are (1)–(2) variation in surface reflectance; (3)–(5) spatial variation in aerosol optical characteristics and geometry; (6) variation in solar zenith angle; and (7) satellite calibration error. The uncertainties related to the model simulations are those in model parameters (8), (9), (10), and (11). Details regarding each factor are described in the main text.

	Error sources												
	Satellite data					Model parameters							Total
Optical properties	(a) Surface reflectance (1), (2)	(b) ρ_c^t (3)–(5)	(c) α (3)–(5)	(d) Solar zenith angle (6)	(e) Satellite Calibration (7)	(f) τ_{a_clear} (8)	(g) $r_{v,1}$ (9)	(h) $r_{v,2}$ (9)	(i) $C_{v,1}$ (9)	(j) $C_{v,2}$ (9)	(k) m_r (10)	(l) Altitude (11)	(m) Total
ω_0 band 9	0.012	0.004	0.001	0.003	0.007	0.002	0.002	0.002	0.002	0.004	0.008	0.009	0.020
ω_0 band 1	0.007	0.003	0.002	0.001	0.003	0.003	0.001	0.002	0.001	0.001	0.003	0.002	0.010
τ_a band 9	0.049	0.032	0.156	0.028	0.054	0.099	0.040	0.026	0.036	0.049	0.062	0.066	0.235
τ_a band 1	0.059	0.041	0.154	0.028	0.054	0.079	0.042	0.043	0.042	0.055	0.061	0.037	0.228

Table 3. Same as Table 2, but for Asia.

	Error sources												
	Satellite data					Model parameters							Total
Optical properties	(a) Surface reflectance (1), (2)	(b) ρ_c^t (3)–(5)	(c) α (3)–(5)	(d) Solar zenith angle (6)	(e) Satellite Calibration (7)	(f) τ_{a_clear} (8)	(g) $r_{v,1}$ (9)	(h) $r_{v,2}$ (9)	(i) $C_{v,1}$ (9)	(j) $C_{v,2}$ (9)	(k) m_r (10)	(l) Altitude (11)	(m) Total
ω_0 band 9	0.012	0.006	0.001	0.003	0.007	0.001	0.004	0.001	0.009	0.004	0.006	0.012	0.023
ω_0 band 1	0.012	0.005	0.003	0.001	0.005	0.003	0.003	0.002	0.005	0.005	0.003	0.002	0.017
τ_a band 9	0.055	0.042	0.397	0.026	0.059	0.111	0.062	0.012	0.121	0.066	0.085	0.081	0.464
τ_a band 1	0.059	0.042	0.284	0.016	0.057	0.096	0.057	0.030	0.120	0.121	0.067	0.020	0.370

3.1.1 Sources of uncertainty

In our method, we assume that the surface reflectance is identical under hazy and clear conditions. We then estimate the daily values of ω_0 and τ_a in $1^\circ \times 1^\circ$ grid points. Therefore, the uncertainties related to the observations are due to the following factors: variations in surface reflectance through (1) variation in the surface reflectance between hazy and clear conditions and (2) bidirectional characteristics of the surface combined with slight variations in the solar zenith angle between hazy and clear conditions; spatial variations in aerosol optical characteristics and geometry (variation in $1^\circ \times 1^\circ$ grid points for (3) ω_0, (4) τ_a, and (5) the geometry); (6) difference in solar zenith angle between clear-sky and hazy conditions; and (7) satellite calibration errors. The inherent error of the radiative transfer calculation in the model simulations is approximately 0.4 % during hazy and clear conditions if the aerosol model is correct (Nakajima and Tanaka, 1988). Therefore, the uncertainties due to the assumptions of the aerosol model are important. Possible sources of uncertainty include uncertainties in the aerosol model parameters: (8) the optical depth of clear conditions, (9) the aerosol size distribution (volume median radius and the ratio of volume concentration between the fine and coarse mode), (10) the real part of the aerosol refractive index, and (11) the dust altitude.

Uncertainties in the surface reflectance, represented by categories (1) and (2), are caused by the variation of the surface reflectance. These variations are evaluated using the MODIS surface reflectance Daily L3 Global 0.05 deg CMG data (MYD09CMG). As described in Sect. 2.4, differences in the TOA reflectance between the hazy and clear conditions are derived from 16 day intervals of data based on the satellite geometry. Therefore, we estimate the variation in the surface reflectance between the hazy and clear conditions from the standard deviation of the surface reflectance at each grid point using the clear-sky data at intervals of 16 days. Because the data with wavelengths in band 9 (0.438–0.448 µm) are not available in MYD09CMG, we use the surface reflectance data with the nearest wavelengths (band 3, 0.459–0.479 µm). The standard deviations of the surface reflectance over the Sahara are 0.0077 (band 1) and 0.0083 (band 3), and those over Asia are 0.0131 (band 1) and 0.0135 (band 3). Uncertainties in the estimation of ω_0 and τ_a are calculated by perturbing the surface reflectance by ±the standard deviation.

Uncertainties in aerosol optical characteristics and geometry, represented by categories (3)–(5), are caused by aerosol optical characeristics and geometry spatial variations in the $1^\circ \times 1^\circ$ grid. These variations are represented by the spread of the scatter plot in the ρ_{clear}^t versus $\Delta\rho^t$ diagram. This spread is also caused by the measurement noise and undetected clouds; thus, categories (3)–(5) include these effects. The uncertainties in ω_0 and τ_a are due to their estimation from the slope (α) and x intercept (ρ_c^t) in the scatter plot by the least-squares method, as shown in Fig. 2. The errors from

α and ρ_c^t caused by the least-squares method are shown in (b) and (c) of Tables 2 and 3, respectively.

For category (6), the standard deviation of the differences in solar zenith angle between clear and hazy conditions in our analysis is 2.3°. The uncertainty in ω_0 and τ_a due to the difference in solar zenith angle of 2.3° is shown in (d) of Tables 2 and 3.

Category (7), concerning satellite calibration error, exhibits uncertainty in the TOA reflectance and ρ_c^t values. Assuming the calibration error of the MODIS satellite is 5 %, the uncertainty in ρ_c^t should also be 5 %. The uncertainty in ω_0 and τ_a due to the satellite calibration is shown in (e) of Tables 2 and 3.

Uncertainties in aerosol model parameters, represented by categories (8)–(10), are calculated by perturbing the aerosol model parameters by the standard deviation, as shown in Table 1. The uncertainties in the model parameters, namely, the aerosol's optical depth during clear conditions (τ_{a_clear}), the fine and coarse modes of the volume median radius (r_{v1}, r_{v2}), the fine and coarse modes of the volume concentration (C_{v1}, C_{v2}), and the real part of the refractive index (m_r), are shown in (f), (g), (h), (i), (j), and (k) of Tables 2 and 3, respectively.

Here, the uncertainties in the aerosol model parameters are derived from the standard deviation of the AERONET retrievals, as shown in Table 1. However, recent aircraft measurements have found a wider range of aerosol size distributions. We performed a sensitivity test with the coarse mode of the volume median radius of 10 µm observed in the Saharan Mineral Dust Experiment (SAMUM: Heintzenberg, 2009). The estimated uncertainty in ω_0 was 0.006 (band 9) and 0.003 (band 1), and the uncertainty in τ_a was 0.06 (band 9) and 0.06 (band 1). These uncertainties do not significantly affect the total uncertainty.

Finally, the uncertainties in dust altitude described by category (11) are addressed by changing the dust layer in the model simulation. In our standard model, we assume that the aerosol layer is at an altitude of 4–8 km. Recent work has found that dust exists at altitudes below 5–6 km (e.g., Johnson and Osborne, 2011; Ryder et al., 2013). We perform the sensitivity test by changing the dust layer to lower (1–5 km) and higher (7–11 km) altitudes. The uncertainty due to the dust altitude is shown in (l) of Tables 2 and 3.

In addition to the uncertainties in the aerosol model discussed above, the spatial variation of ozone concentration can be a source of uncertainty in our radiative transfer simulation. The annual average of total-column ozone over the northern part of the Sahara is approximately 270 DU, while that over the southern part is approximately 310 DU (WMO, 2011). We performed a sensitivity test with the total-column ozone of 270 DU and 310 DU, but the uncertainty did not affect the total uncertainty discussed above.

3.1.2 Uncertainty in the estimations

The uncertainty components and total uncertainty in the estimation of ω_0 and τ_a over the Sahara and Asia are shown in Tables 2 and 3, respectively. When estimating ω_0, the largest contribution to the total uncertainty is the variation in surface reflectance (categories 1 and 2), as shown in (a) of Tables 2 and 3. The largest contribution to the total uncertainty in the estimation of τ_a is the spatial variation in aerosol optical characteristics (categories 3–5), as shown in (c) of Tables 2 and 3.

We should note that the uncertainty in ω_0 caused by the variation in surface reflectance increases for smaller τ_a values because the uncertainties in ρ_c^t (the x intercept in the ρ_{clear}^t versus $\Delta\rho^t$ diagram) increase with decreasing τ_a, for which the absolute value of the slope (α) decreases. For this reason, we use only MODIS satellite data with $\tau_a > 0.5$ in order to reduce the uncertainties in this study's estimation of ω_0.

The spatial distribution of the total uncertainties in the estimation of ω_0 and τ_a over the Sahara and Asia are shown in Figs. 4 and 5, respectively. The total uncertainty of ω_0 becomes large over the northwestern region of the Sahara because the dust's optical depth τ_a is not large enough. The total uncertainty of τ_a becomes large over the southern region, which contains AERONET sites. In this region, the uncertainties in categories (3)–(5) are large, most likely because the estimated value of τ_a is large.

In Asia, the total uncertainty in ω_0 is larger in the east of the Takla Makan Desert compared with that over the Takla Makan Desert region (Fig. 5) because uncertainties due to the variation in the surface reflectance (categories 1 and 2) and to the dust altitude (categories 11) are large there. As in the case of the Sahara, uncertainty in ω_0 due to the variation in surface reflectance is large over the regions where τ_a is small. By contrast, the uncertainty in τ_a is large over the Takla Makan Desert.

As shown in Table 2 (m) and Table 3 (m), the total uncertainty in ω_0 over the Sahara (Asia) is 0.020 and 0.010 (0.023 and 0.017) for bands 9 and 1, respectively, and the total uncertainty in τ_a is 0.235 and 0.228 (0.464 and 0.370) for bands 9 and 1, respectively. The 5–95 % range of the spatial distribution of ω_0 over the Sahara (Asia), as investigated in Sect. 3.3, is approximately 0.90–0.94 and 0.96–0.99 (0.87–0.94 and 0.89–0.97) for bands 9 and 1, respectively, and that of τ_a over the Sahara (Asia) is approximately 0.8–1.4 and 0.8–1.7 (0.7–2.0 and 0.7–1.9) for bands 9 and 1, respectively. Therefore, the total uncertainties shown in Tables 2 and 3 are suitably minor compared with the spatial distribution over the Sahara and Asia.

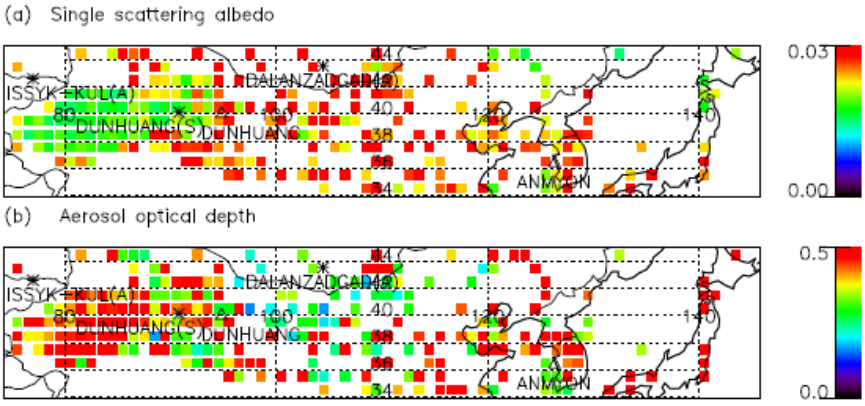

Fig. 5. This figure is identical to Fig. 4, but shows the results for Asia.

3.2 Comparison of dust's optical properties with ground observations

3.2.1 The Sahara

We evaluate our method by comparing the calculated ω_0 and τ_a values with ground observations. We use Level 2.0 inversion data for ω_0 (http://aeronet.gsfc.nasa.gov) and the direct sun algorithm for τ_a (O'Neill et al., 2003) at the AERONET site over the Sahara (the site locations are indicated in Fig. 4). In Fig. 6, the ω_0 and τ_a values estimated with our method are compared with the AERONET data observed on the same day. We use the AERONET ω_0 observed at the nearest time to the MODIS observation time. We also use the AERONET τ_a data averaged over 30 min before and after the MODIS observation time. The error bars in Fig. 6 represent the total uncertainty calculated at each point described in Sect. 3.1. The AERONET data at 0.440 µm and 0.675 µm are compared with MODIS bands 9 (0.438–0.448 µm) and 1 (0.620–0.670 µm), respectively.

The ω_0 data from the ground observations are consistent with our estimations, as shown in Fig. 6. The spread in the AERONET data is larger than that in the MODIS data, most likely because the former is in the form of point observations, while the latter is in the form of spatial averages over $1^\circ \times 1^\circ$. However, the estimated τ_a values are larger than those from the AERONET observations, especially for a small τ_a. Although our method tends to overestimate τ_a, our estimations correlate with the AERONET observations (the correlation coefficients are 0.462 and 0.311 at bands 9 and 1, respectively).

In general, when the τ_a of the MODIS data is consistent with that of the AERONET observations (points around the $y = x$ line), the error bars of the MODIS data tend to be small, as shown in Fig. 6. On the other hand, when the τ_a of the MODIS data is larger than that of the AERONET observations (points well above the $y = x$ line), the error bars tend to be large. Therefore, we calculate the regression line by considering the error bars of τ_a in Fig. 6 as the "measurement error" and giving larger (smaller) weights to the data with smaller (larger) error bars. The regression line that considers the measurement error of τ_a (red line in Fig. 6) is more consistent with the AERONET observations than the line that does not consider measurement error (blue line).

As discussed in Sect. 3.1, the uncertainties in τ_a are mainly caused by the spread in the ρ^t_{clear} versus $\Delta\rho^t$ diagram, as shown in Table 2 (c). As shown in Fig. 6, the τ_a values estimated from MODIS show a large spread. In general, the data with small slopes α (and small τ_a) tend to be rejected by the statistical test in our method using the null hypothesis of $\alpha = 0$ because a very small α is indistinguishable from zero. On the other hand, AERONET data with a small τ_a are not rejected in Fig. 6. Therefore, one of the reasons for the overestimation of τ_a in the MODIS data compared with the AERONET observations is that the data with a small τ_a are not often sampled in Fig. 6.

We should note that recent work has found that AERONET retrievals of ω_0 are different from those of aircraft measurements (Johnson and Osborne, 2011; Müller et al., 2010, 2012). This finding might call into question the ability of AERONET to provide reliable ω_0, but filter-based aircraft measurements of absorption have their own problems, artifacts and uncertainties (Johnson and Osborne, 2011; Bond et al., 2013).

3.2.2 Asia

Ground observations are available for the AERONET sites at Dalanzadgad and Issyk-Kul and for the SKYNET site at Dunhuang, as shown in Fig. 9. However, the observational data synchronised with our MODIS data are available only at Dunhuang (a SKYNET site) on 25 April 2004. We use ω_0 and τ_a from the SKYNET data derived by Hashimoto et al. (2012) for our analysis. Because the radiation bands of the MODIS satellite are not the same as those of SKYNET, we use SKYNET data at 0.400 µm and 0.500 µm and interpolate

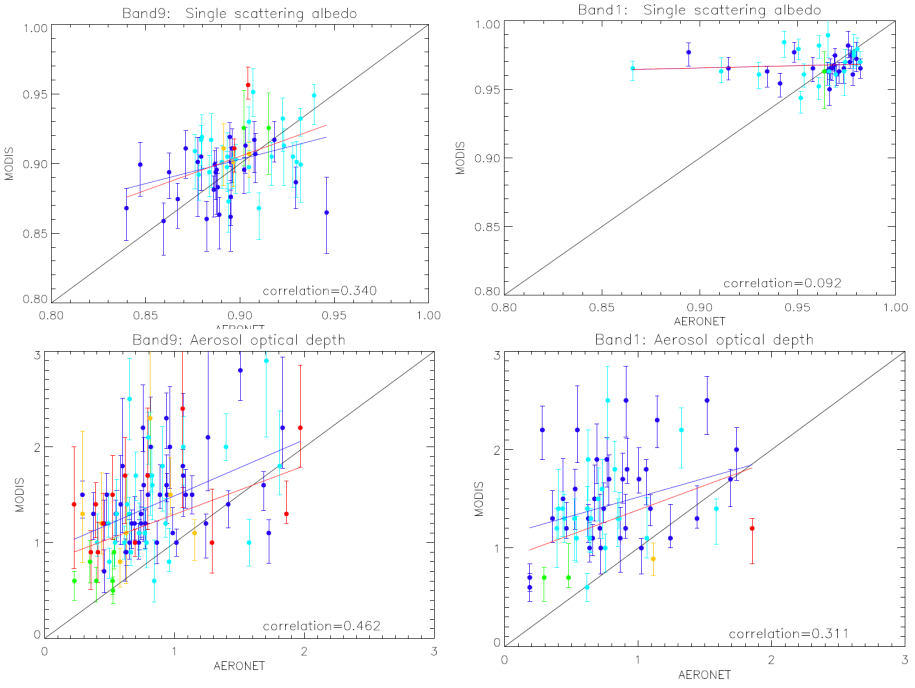

Fig. 6. Comparison of the single scattering albedo (ω_0) and optical depth (τ_a) values we estimated from the MODIS satellite data and the model simulations with the AERONET ground observation data. The error bars represent the total uncertainty described in Sect. 3.1. We sample the results of grid boxes that include the AERONET sites Agoufou (blue), Banizoumbou (light blue), Saada (green), Tamanrasset_INM (orange), and Tamanrasset_TMP (red). The lines indicate the regression by considering the error bars as the "measurement error" (red) and not considering the measurement error (blue), the details of which are described in the main text.

them to determine the value at 0.443 µm for comparison with our data at MODIS band 9 (0.438–0.448 µm, midpoint = 0.443 µm). We also use SKYNET data at 0.675 µm for comparison with our MODIS band 1 (0.620–0.670 µm) data.

Our estimates of ω_0 using the MODIS satellite data at Dunhuang on 25 April 2004 are 0.93 (band 9) and 0.99 (band 1), while those using the SKYNET data are 0.89 (band 9) and 0.94 (band 1). Our estimates of τ_a at Dunhuang on that day are 1.60 (band 9) and 1.00 (band 1) using MODIS data, while those using SKYNET data are 0.46 (band 9) and 0.45 (band 1). Our calculated results for ω_0 slightly overestimate the SKYNET observations, and those for τ_a are larger than the observation results.

In addition to using the SKYNET observations, we compare our estimates of ω_0 with other observations, although these comparisons are not synchronised. The ω_0 values at 0.5 µm reported at Dunhuang during the years 1998–2000 were 0.89 (Kim et al., 2005) and 0.90 (Kim et al., 2004), and those at Anmyon in the years 1998 and 2000 were 0.86 (Kim et al., 2005) and 0.87 (Kim et al., 2004). Furthermore, the ω_0 at 0.5 µm reported at Anmyon was 0.91 on 7 April 2000 (Sohn et al., 2007). Our estimation of the ω_0 around Dunhuang is approximately 0.90–0.95, and our estimation of ω_0 around Anmyon is approximately 0.86–0.93. Therefore, our ω_0 results are consistent with or slightly larger than those in previous studies.

In conclusion, our estimation of ω_0 in the Asian region is nearly consistent with the ground observations; τ_a, by contrast, is overestimated. These results are similar to those obtained in the Sahara region.

3.2.3 Effect of overestimating optical depth on the estimation of the single scattering albedo

As described in Sects. 3.2.1 and 3.2.2, our estimation of ω_0 is generally consistent with existing observations, while our estimation of τ_a is overestimated. Therefore, the τ_a estimated from MODIS may not give useful information about dust's optical properties. In addition, this overestimation of τ_a may affect the estimation of ω_0, so we validate this relationship in Fig. 7. Because the overestimation of τ_a is generally caused by the overestimation of α, as demonstrated in Fig. 2, we reduce the value of α by two standard deviations and estimate the value of ω_0. As shown in Fig. 7, this reduction of α does not affect the estimation of ω_0 in our method. This result is entirely consistent with the conceptual framework shown in Fig. 1 and the LUT shown in Fig. 3: an increase in τ_a changes α, but has little impact on the critical TOA reflectance. Thus, once the critical surface reflectance is obtained, ω_0 is relatively well constrained. Therefore, it is reasonable to assume

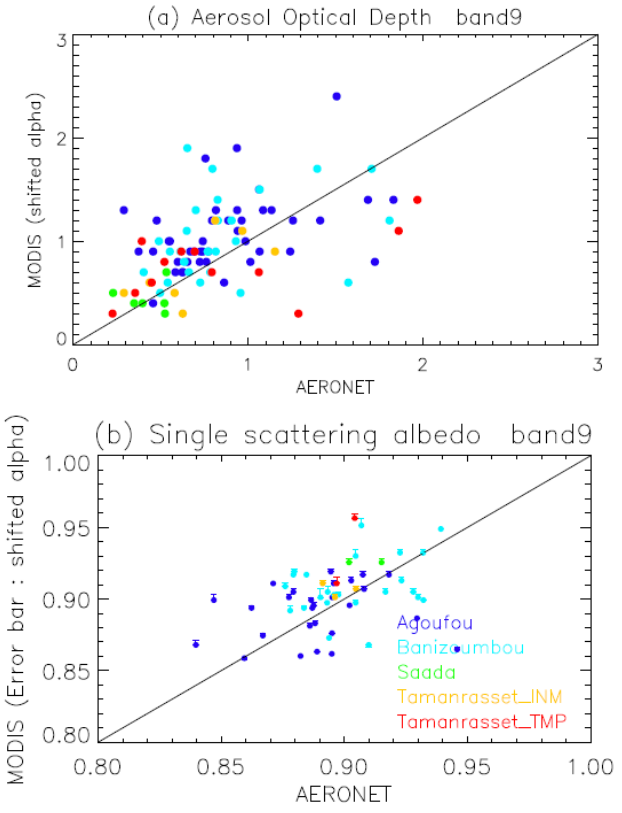

Fig. 7. The effect of overestimating the aerosol optical depth (τ_a) on the estimation of the single scattering albedo (ω_0) in band 9. The horizontal axis represents the observed aerosol optical properties at the AERONET sites (the colours are the same as those in Fig. 6). **(a)** τ_a calculated by reducing the slope α in Fig. 2 by two standard deviations. **(b)** The same ω_0 as in Fig. 6, but the error bars represent the difference between the value in Fig. 6 and the ω_0 value estimated by reducing α by two standard deviations. The standard deviations are estimated from the uncertainty in α as described in Sect. 3.1.

that the overestimation of τ_a does not affect the estimation of ω_0, and that ω_0 is consistent with the ground observations.

3.3 Spatial distribution of aerosol's optical properties over the Sahara and Asia

The spatial distributions of optical properties over the Sahara and Asia are shown in Figs. 8 and 9, respectively. The spatial resolution in these figures is $1° \times 1°$, with the time average taken using daily ω_0 and τ_a values estimated with the 2003–2011 MODIS data. We take the temporal average of ω_0 and τ_a weighted by the total uncertainty at each grid.

As shown in Figs. 8 and 9, neither ω_0 nor τ_a are spatially uniform. Compared with the magnitudes of the spatial variations in these figures, the total uncertainties estimated in Sect. 3.1 are suitably small in both the Sahara and Asia. Therefore, we can consider the spatial variations shown in Figs. 8 and 9 to be significant. However, as previously noted, while the retrieval of ω_0 appears relatively robust, there appears to be a significant overestimate of τ_a when compared with AERONET measurements.

To investigate the factors determining the spatial distributions of dust's optical properties, we compare the spatial distributions of dust's optical properties with that of surface reflectance. We use the bihemispherical reflectance (white-sky albedo) of the MODIS albedo product 16-Day L3 data (MCD43C3), and we take the time average using the same term as that employed with the MODIS data used to determine ω_0 and τ_a as described in Sect. 2.2. Because data with wavelengths in band 9 (0.438–0.448 µm) are not available in MCD43C3, we use band 3 data (0.459–0.479 µm), which has the wavelength range closest to that of band 9. Note that we do not use the MODIS products for the surface albedo in our the estimation of ω_0 and τ_a; instead, we use the TOA reflectance of clear and hazy conditions (ρ^t_{clear} and $\Delta\rho^t$) in our analysis.

Fig. 10 shows the scatter plot of ω_0 and the surface reflectance. ω_0 increases in both the Sahara and Asia when the surface reflectance increases. The correlation coefficients between ω_0 and the surface reflectance over the Sahara are 0.63 and 0.76 for bands 9 and 1, respectively; over Asia, they are 0.54 and 0.68 for bands 9 and 1, respectively. These correlations are both significant, but the correlation of the data for the Sahara is higher than that of the data for Asia. The upper end of the ω_0 in Asia is approximately the same as that in the Sahara, while there are many points with ω_0 values lower than those in the Sahara (Fig. 10). As shown in the Introduction, previous studies suggest that the observed ω_0 over the Sahara is higher than that over Asia. These results are consistent with our results shown in Fig. 10, in which the average of ω_0 over the Sahara is higher than that over Asia.

One may inquire whether the correlation between ω_0 and the surface reflectance in Fig. 10 was caused by errors inherent in this method. Possible sources of errors related to the surface reflectance are (i) the spread in the scatter plot in Fig. 2, (ii) the errors in the sensor calibration, and (iii) the nonlinearity of the scatter plot in Fig. 2. The error source of (i) is investigated by categories (3)–(5) and that of (ii) is investigated by category (7), as described in Sect. 3.1. The error source of (iii) is treated by creating the four different LUTs for the four different ρ^t_{clear} ranges, as described in Sect. 2.4. Therefore, the correlation between ω_0 and the surface reflectance in Fig. 10 may not be spurious structural bias.

One possible reason for the correlation between ω_0 and the surface reflectance could be that the ω_0 of airborne dust is determined by the mineral composition of the ground surface in arid areas. If the dust on a surface with high reflectivity is transported to the atmosphere, ω_0 should become large. As shown in Fig. 8a, the spectral variation in ω_0 is larger in the western part of the Sahara than in the eastern part. This result is consistent with the feature of spectral variation in the surface reflectance shown in Fig. 8c.

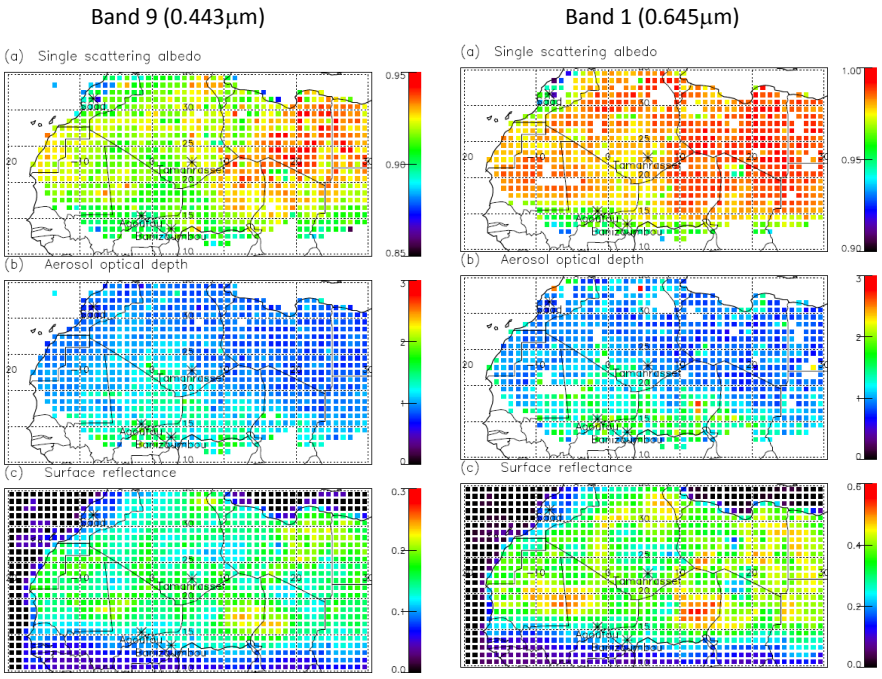

Fig. 8. The spatial distribution of **(a)** single scattering albedo ω_0, **(b)** aerosol optical depth τ_a, and **(c)** surface reflectance in the Sahara. **(a)** and **(b)** are estimated by our method using the 9 yr (2003–2011) May–August data from MODIS and model simulations. **(c)** is obtained from the MODIS albedo 16-Day L3 data product (MCD43C3, bihemispherical reflectance). The spatial resolution is $1^\circ \times 1^\circ$, and the results are based on the time average. The number of MODIS data points in the white grid boxes that satisfy the conditions described in Section 2 is less than two. The AERONET sites of Agoufou, Banizoumbou, Saada, and Tamanrasset are also shown.

We should note that there are regions that are not dust sources. In addition, dust can be transported over a considerable distance. The areas shown in Figs. 8 and 9 contain the vegetation and bedrock, which cannot be considered as the dust source regions. In these areas, the ω_0 we estimated may not be related to the dust on the surface. To identify regions that can be dust source regions, we compared the spatial distribution of the surface reflectance with the soil map of FAO/Unesco (FAO, 1991) as shown in Fig. 11. The soil properties in the Sahara and Asia regions mainly consist of dunes/shifting sand, rock debris, Yermosols, Lithosols, Regosols, Arenosols, Kastanozems, and Cambisols (Fig. 11). The regions with dunes/shifting sand and Yermosols can be considered the dust source regions (FAO, 1991). When we compare the soil maps with the spatial distribution of the surface reflectance (Figs. 8 and 9), the regions with these categories (dunes/shifting sand and Yermosols) tend to have high surface reflectance, especially at band 1.

The regions with rock debris and Lithosols tend to have a low surface reflectance of less than approximately 0.12 (band 9) and 0.25 (band 1). For these regions, we cannot discuss the relationship between the surface mineral composition and ω_0 because the atmospheric aerosol should not be related to the surface reflectance.

In addition to the relationships between ω_0 and the surface reflectance, the relationships between ω_0 and τ_a are also shown in Fig. 10. ω_0 decreases for large τ_a values in the Sahara (the correlation coefficients are -0.51 and -0.36 for bands 9 and 1, respectively). On the other hand, the correlations between ω_0 and τ_a are very small in Asia (-0.10 and 0.03 for bands 9 and 1, respectively).

In the theory of light scattering by small particles, ω_0 decreases for larger particle radii at a constant refractive index. The correlation between ω_0 and the particle radius becomes larger at smaller wavelengths. Therefore, one possible reason for the good correlation between ω_0 and τ_a over the Sahara (especially at band 9), although other reasons exist, is that the wind is strong and/or there are sufficient dust sources in regions with large dust optical depths. In these regions, large dust particles are often transported to the atmosphere, decreasing the value of ω_0. The relationship between ω_0 and τ_a shown in Fig. 10 might be consistent with recent work by Ryder et al. (2013), who found that particle size decreased with dust age during transport. Because smaller particles contribute to a larger ω_0, this would suggest an increase in ω_0 as τ_a decreases with dust age.

It should be noted that we cannot validate the spatial distribution of aerosol optical properties and the relationship between ω_0, τ_a, and the surface reflectance because

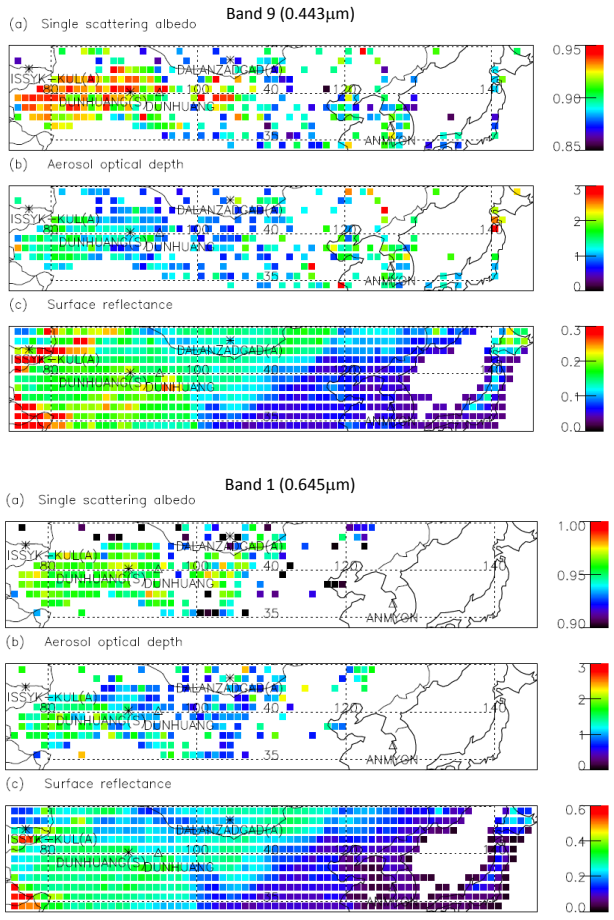

Fig. 9. This figure is identical to Fig. 8 but shows the results for Asia. The months used for the estimation are March-May because the season of dust activity is different than in the Sahara. The ground observation sites for (A) AERONET and (S) SKYNET are also shown. The triangle indicates the observation sites from Kim et al. (2004, 2005) and Sohn et al. (2007).

the number of ground observations is limited (only four AERONET sites). To investigate the relationship more carefully, we compare the relationship between ω_0 and τ_a using the daily $1° \times 1°$ MODIS data and AERONET data. As shown in Fig. 12, the relationships of ω_0 and τ_a are consistent enough between MODIS and AERONET data. The correlations between ω_0 and τ_a are not significant except for AERONET Agoufou at band 1. Data are only available for the Agoufou and Banizoumbou AERONET sites because the matched data between MODIS and AERONET are very limited; thus, we cannot find the significant difference between the satellite retrievals and the ground observation at this stage. Increasing the number of observation sites would help us validate the spatial distribution and the relationships among the aerosol optical properties.

3.4 Comparison of dust's optical properties between the Sahara and Asia

Figure 10 shows the good correlations between ω_0 and surface reflectance and between ω_0 and τ_a over the Sahara. Therefore, the ω_0 of airborne dust is determined by the mineral composition of the surface and by the optical depth. By contrast, the correlation coefficient between ω_0 and the surface reflectance is slightly smaller in Asia, and the spread of ω_0 values is large compared with that of the Sahara. In addition, the correlation coefficient between ω_0 and τ_a is insignificant in Asia. Accordingly, there should be additional factors affecting ω_0 in Asia.

To investigate the factors that cause the different features of ω_0 in Asia, we compare the spatial distribution of ω_0 to that of the dust emission flux as determined by Mukai et al. (2004). The dust emission flux averaged over 1981–2001 in Mukai et al. (2004) was estimated using a global aerosol transport model (Takemura et al., 2000, 2002a, b). Figure 13 shows the region with large dust emissions in Fig. 4 of Mukai et al. (2004), which can be considered a dust source region and is indicated by red circles. This region is also consistent with the region containing the large vertical dust flux estimated in Kang et al. (2011) on 30 March 2007. As shown in Fig. 13, the dust source region in Mukai et al. (2004) is in good agreement with the region identified as having large ω_0 values in our study. This region also corresponds to the Takla Makan and Gobi deserts on geological maps.

In general, dust is transported eastward from the source region at these latitudes (e.g., Huang et al., 2008). We investigate the daily feature of the OMI aerosol index and confirm that the dust clouds formed around the source region are often transported eastward to eastern China, Korea, or Japan (not shown).

The spatial features of the dust aerosol's ω_0 value, as shown in Fig. 13, are consistent with the findings of Kim et al. (2004, 2005), in which the ω_0 values observed around dust source regions such as Dunhuang were large compared with the ω_0 values in areas located farther from the source region, such as Anmyon, Gosan, and Amami-Oshima. Coal-burning smoke mixed with dust was also observed in the regions surrounded by a blue box in Fig. 13 (Herman et al., 1997). Mukai et al. (2004) also estimated that carbonaceous and dust aerosols were transported around the region with the blue box in Fig. 13.

It is well known that coal-burning smoke and carbonaceous aerosols have relatively large absorptivities compared with dust aerosols (Forster et al., 2007). In our results, the ω_0 values around the blue box in Fig. 13 are small compared with those in the dust source region. Therefore, it is reasonable to assume that the dust transported from the source region is contaminated by coal-burning smoke and/or carbonaceous aerosols around the downstream region indicated by the blue box in Fig. 13. These features are also evident in the scatter plots shown in Fig. 10. In Asia, the spread of the

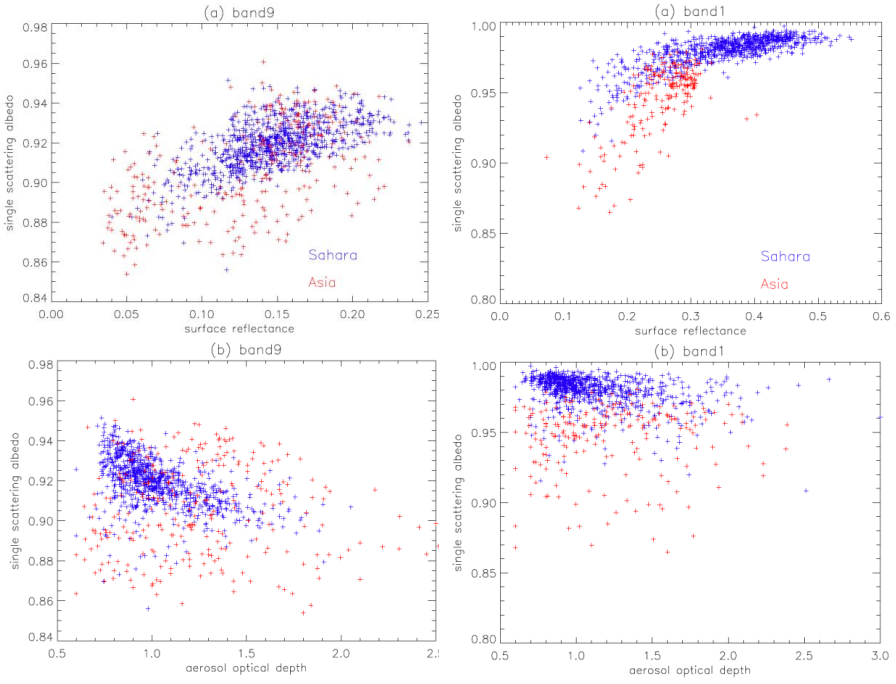

Fig. 10. Scatter plot between **(a)** the single scattering albedo ω_0 and the surface reflectance and **(b)** ω_0 and the aerosol optical depth τ_a. The red dots indicate the results in Asia and the blue dots indicate those in the Sahara. Each dot in the scatter plot corresponds to the value for 1° × 1° of resolution, as shown in Figs. 8 and 9. The MODIS data used for the analysis are the same as those used in Figs. 8 and 9.

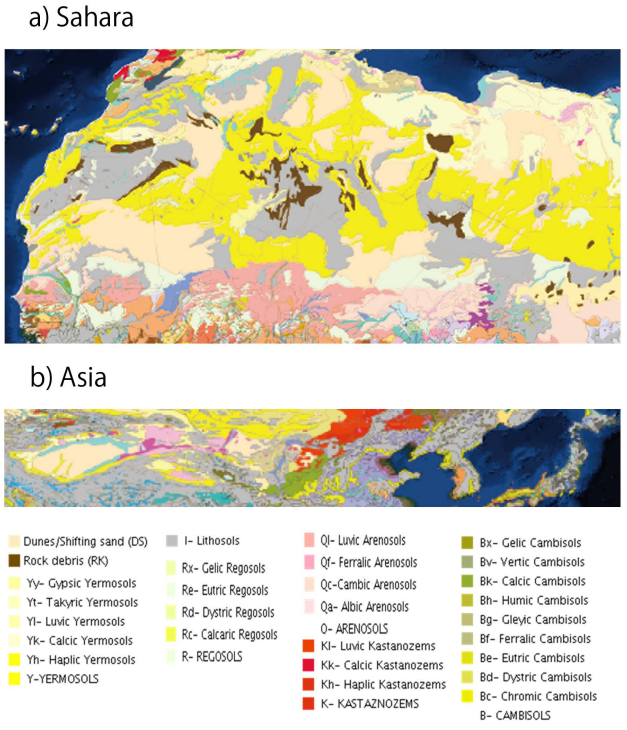

Fig. 11. Soil map for **(a)** the Sahara and **(b)** Asia using the database of FAO/Unesco (FAO, 1991).

ω_0 scatter plot is large compared with that in the Sahara, and the ω_0 values in Asia are generally smaller than those in the Sahara. The lack of correlation between ω_0 and τ_a also suggests that the ω_0 values in Asia are not strongly influenced by the dust's optical depth or particle radius, although these are important factors in determining the ω_0 values in the Sahara.

Another possible interpretation of Figs. 10 and 13 is that we sample only the carbonaceous aerosols (or aerosols other than dust) around or at the east side of the blue box in Fig. 13. To test this hypothesis, we count the number of samples of daily data that satisfy the criteria in the analysis (Fig. 14). In the present study, we use the daily data with the TOMS aerosol index (AI) > 3 for the dust conditions in spring (from March to May) as described in Sect. 2. Figure 14 shows the number of samples of daily data with the TOMS AI > 3 in spring and the other seasons: winter (from December to February), summer (from June to August), and autumn (from September to November).

As shown in Fig. 14, the number of samples with TOMS AI > 3 is large in spring, especially around the Takla Makan Desert and the east side of the Gobi Desert. However, the number of samples in winter, summer, and autumn is very small, except around the Takla Makan Desert in summer. Dust storms often occur in spring (Herman et al., 1997), and Mukai et al. (2004) reported that the optical thickness of dust aerosols becomes large from March to May in these regions.

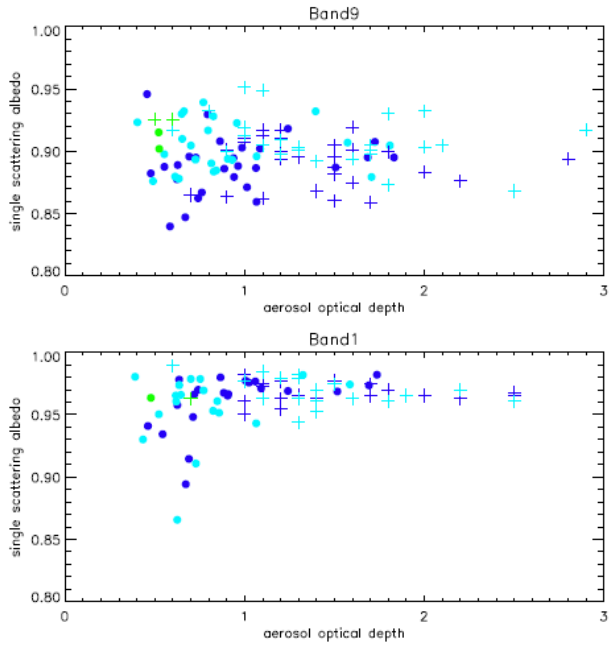

Fig. 12. Scatter plot of the single scattering albedo ω_0 and the aerosol optical depth τ_a using the daily $1^\circ \times 1^\circ$ MODIS data (cross) and the AERONET data (dot). The colours are the same as those in Fig. 6. We only show the matched-up data between MODIS and AERONET. The correlations between ω_0 and τ_a of MODIS (AERONET) are -0.422 (0.227) and -0.016 (0.508) for Banizoumbou (light blue) and Agoufou (blue) at band 1, and -0.337 (-0.018) and -0.09 (0.166) at band 9. The numbers of the matched-data at Banizoumbou and Agoufou at band 1 (band 9) are 21 and 18 (24 and 27), respectively.

On the other hand, Mukai et al. (2004) suggested that the carbonaceous aerosols are emitted and transported more in winter (from December to February) than in other seasons in the eastern part of the Asian region. However, the number of samples with TOMS AI > 3 is small in winter compared with that in spring (Fig. 14). Therefore, it is likely that the majority of the daily data with TOMS AI > 3 in the spring used for the analysis corresponds to the dust aerosols or a mixture of dust and other aerosols.

4 Summary

In this study, we develop a method for estimating the optical properties of aerosols, including single scattering albedo (ω_0) and optical depth (τ_a), with a daily $1^\circ \times 1^\circ$ resolution. This approach is based on the critical surface reflectance method developed by Kaufman et al. (1987). By estimating τ_a and ω_0 simultaneously, we can estimate the spatial distributions of ω_0 over inland desert areas for which limited observations are available. We estimate the spatial distributions of ω_0 and τ_a over the Sahara and Asia using nine years of MODIS satellite data from bands 9 (0.438–0.448 µm) and 1 (0.620–0.670 µm).

Our method uses model simulations of radiative transfer to estimate the aerosol's optical properties from the critical surface reflectance obtained with the satellite data. To validate the significance of our results, we also investigate the uncertainties of our estimation based on possible error sources related to the satellite data and model simulations. We calculate the uncertainties in ω_0 over the Sahara (Asia) to be approximately 0.020 and 0.010 (0.023 and 0.017) for bands 9 and 1, respectively, while the uncertainty in τ_a is approximately 0.235 and 0.228 (0.464 and 0.370) for bands 9 and 1, respectively.

To validate our results, we compare our estimations of ω_0 and τ_a with ground observations and find that ω_0 is consistent with the observations, whereas τ_a is significantly overestimated. This overestimation is most likely due to the large spread in the estimated τ_a values and the fact that small τ_a values tend to be rejected by the significance test. However, the theoretical framework developed here confirms that the overestimation of τ_a does not affect the results for ω_0.

We find significant spatial distributions of ω_0 and τ_a over the Sahara and Asia, as shown in Figs. 8 and 9. To interpret the features of these spatial distributions, we investigate the relationship between ω_0, τ_a, and the surface reflectance (Fig. 10), and we observe a good correlation between ω_0 and the surface reflectance in both the Sahara (0.63 and 0.76 for bands 9 and 1, respectively) and Asia (0.54 and 0.68 for bands 9 and 1, respectively). The spread of ω_0 is larger and the value of ω_0 is smaller in Asia than in the Sahara when the surface reflectance is kept constant (Fig. 10). In addition, the correlation between ω_0 and τ_a is significant in the Sahara (with correlation coefficients of -0.51 and -0.36 for bands 9 and 1, respectively) but is very small in Asia (-0.10 and 0.03 for bands 9 and 1, respectively).

The good correlations between ω_0 and the surface reflectance and between ω_0 and τ_a in the Sahara suggest that the temporal average of ω_0 is largely affected by the underlying mineral composition and the optical depth of the airborne dust, although there should be many complicating factors in determining the individual ω_0.

On the other hand, the relationships between ω_0, τ_a, and the surface reflectance in Asia are less clear than those in the Sahara, and the ω_0 values are generally smaller than those in the Sahara (Fig. 10). In terms of the spatial distribution of ω_0, the regions with high ω_0 value correspond well with the Takla Makan and Gobi Desert regions as well as the source region of dust aerosols estimated by a global aerosol transport model in Mukai et al. (2004), as shown by the red circles in Fig. 13. In addition, the ω_0 values are small around the regions in which coal-burning smoke was observed (Herman et al., 1997), and the carbonaceous aerosols were transported in a global model (Mukai et al., 2004), as shown by the blue box in Fig. 13. Considering that anthropogenic aerosols have relatively large absorptivity and therefore smaller ω_0 values

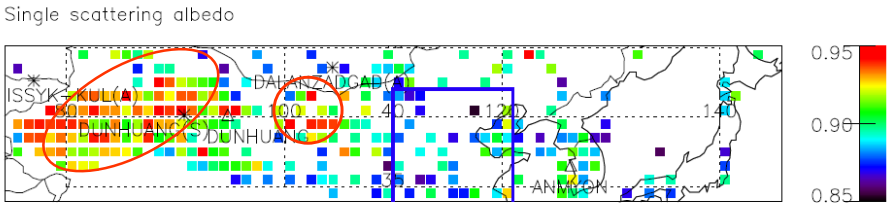

Fig. 13. This figure is identical to Fig. 9a in its depiction of the spatial distribution of the single scattering albedo in band 9 over Asia, but it shows the areas of typical behaviours of particular aerosols reported in previous studies, denoted by the red circles and blue box. The red circles correspond to the regions with the large dust emissions calculated by a global aerosol transport model (Mukai et al., 2004). The blue box corresponds to the region in which coal-burning smoke mixed with dust was observed with the Ozone Monitoring Instrument (Herman et al., 1997).

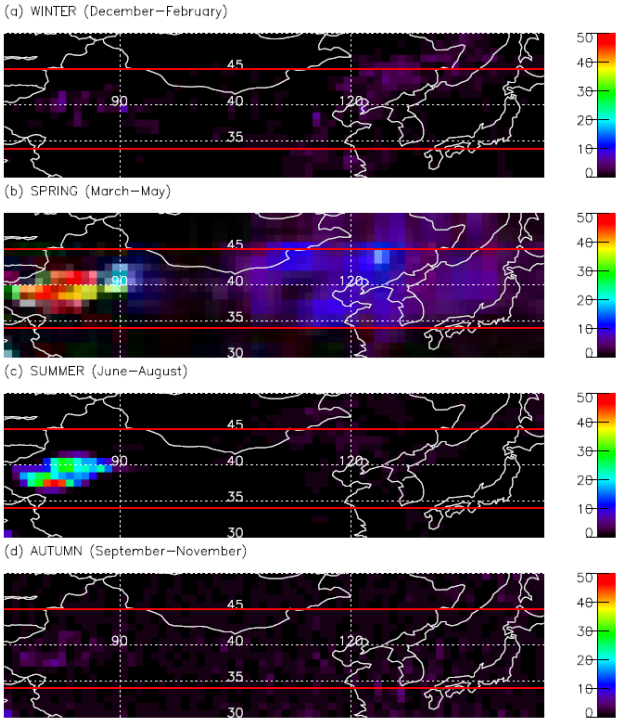

Fig. 14. Number of samples of daily data with TOMS aerosol index (AI) > 3 in **(a)** winter (December–February), **(b)** spring (March–May), **(c)** summer (June–August), and **(d)** autumn (September–November) using the 2005–2009 data. The region used for the analysis of dust optical properties in Figs. 9, 10, 13 is indicated by the red lines.

compared with dust aerosols (Forster et al., 2007), our results indicate that dust aerosols are contaminated by these anthropogenic aerosols in adjacent regions.

Our analysis reveals distinct differences in the spatial distributions of dust properties in the Saharan versus Asian regions. Our results concerning dust's optical properties may be useful in understanding the roles of dust aerosols in Earth's climate system, as discussed in Sect. 1. The spatial distribution of ω_0 we estimated over Asia could also be helpful in understanding the mixing processes of dust and anthropogenic aerosols, such as smoke and carbonaceous aerosols. Finally, our method allows the optical properties of aerosols to be estimated on a daily basis with spatial distributions of $1^\circ \times 1^\circ$ when satellite data with appropriate conditions are available. For instance, the time evolution of aerosol optical properties might be investigated if combined with information on dust age (e.g., Ryder et al., 2013). If the quality and quantity of satellite data are improved in the future, analyses using the method proposed in this paper will advance knowledge regarding the uncertainties of aerosol's optical properties.

Appendix A

Interpretation of the proposed method with approximated equations

To interpret our method for the estimation of dust aerosol's optical properties, we derive the relationship between [ω_0, τ_a] and [ρ_c^t, α] with approximated equations that can be obtained under simple conditions. The interpretation of the model simulations using approximated equations for the relationship between ω_0 and ρ_c^t was given in Kaufman (1987), so we focus our attention on the interpretation of τ_a. The relationship between the TOA reflectance (ρ^t) and the reflectance of a Lambert surface (ρ_g) is the following (Chandrasekhar, 1960):

$$\rho^t = \rho_0^t + T_d T_u \rho_g / (1 - s\rho_g), \quad \text{(A1)}$$

where ρ_0 is the reflectance of the atmosphere if the ground is non-reflecting ($\rho_g = 0$), T_d is the total transmittance from the top of the atmosphere to the ground, T_u is the total transmittance from the ground to the top of the atmosphere, and s is the fraction of the upward flux reflected back to the surface by the atmosphere. An expression for atmospheric transmission (T_d and T_u) is formulated as (Meador and Weaver, 1980):

$$T_d = \exp\left\{\{-\sec\theta_0\}\left\{\tau_a\left[1 - \omega_0\left(1 - \beta^a\right)\right] + \tau_m/2\right\}\right\}, \quad \text{(A2)}$$

$$T_{\mathrm{u}} = \exp\left\{\{-\sec\theta\}\left\{\tau_{\mathrm{a}}\left[1-\omega_0\left(1-\beta^{\mathrm{a}}\right)\right]+\tau_{\mathrm{m}}/2\right\}\right\}, \quad \text{(A3)}$$

where τ_{m} is the molecular optical depth, τ_{a} is the aerosol optical depth, and β^{a} is the aerosol backscattering fraction (Coakley and Chylek, 1974). By substituting Eqs. (A2)–(A3) in Eq. (A1):

$$\rho^{\mathrm{t}} = \rho_0^{\mathrm{t}} + \frac{\rho_{\mathrm{g}}}{\left(1-s\rho_{\mathrm{g}}\right)} \quad \text{(A4)}$$
$$\exp\left\{\left\{-\tau_{\mathrm{a}}\left[1-\omega_0\left(1-\beta^{\mathrm{a}}\right)\right]-\tau_{\mathrm{m}}/2\right\}\{\sec\theta_0+\sec\theta\}\right\}.$$

The TOA reflectance during clear conditions can be formulated in the same manner:

$$\rho^{\mathrm{t}}_{\mathrm{clear}} = \rho^{\mathrm{t}}_{0\_\mathrm{clear}} + \frac{\rho_{\mathrm{g}}}{\left(1-s\rho_{\mathrm{g}}\right)} \quad \text{(A5)}$$
$$\exp\left\{\left\{-\tau_{\mathrm{a\_clear}}\left[1-\omega_0\left(1-\beta^{\mathrm{a}}\right)\right]-\tau_{\mathrm{m}}/2\right\}\{\sec\theta_0+\sec\theta\}\right\},$$

where τ_{clear} and $\tau_{\mathrm{a\_clear}}$ are the total and aerosol optical depths during clear conditions, respectively, and $\rho^{\mathrm{t}}_{0\_\mathrm{clear}}$ is the same as ρ_0^{t} but during clear conditions. The relationship between $\Delta\rho^{\mathrm{t}}$ and $\rho^{\mathrm{t}}_{\mathrm{clear}}$ is then calculated using Eqs. (A4) and (A5):

$$\Delta\rho^{\mathrm{t}} = \rho^{\mathrm{t}} - \rho^{\mathrm{t}}_{\mathrm{clear}} = \alpha\rho^{\mathrm{t}}_{\mathrm{clear}} + \beta. \quad \text{(A6)}$$

α and β in Eq. (A6) are calculated as follows:

$$\alpha = \exp\left\{-(\sec\theta_0+\sec\theta)\left(\tau_{\mathrm{a}}-\tau_{\mathrm{a\_clear}}\right)\left[1-\omega_0\left(1-\beta^{\mathrm{a}}\right)\right]\right\}-1, \quad \text{(A7)}$$

$$\beta = \rho_0^{\mathrm{t}} \quad \text{(A8)}$$
$$-\left\{-\exp\left\{-(\sec\theta_0+\sec\theta)\left(\tau_{\mathrm{a}}-\tau_{\mathrm{a\_clear}}\right)\left[1-\omega_0\left(1-\beta^{\mathrm{a}}\right)\right]\right\}\right\}$$
$$\rho^{\mathrm{t}}_{0\_\mathrm{clear}}.$$

Here, we assume that the values of ω_0 and β^{a} are remain constant in both hazy and clear conditions. In addition, the variation of $s\rho_{\mathrm{g}}$ due to an additional aerosol layer is ignored because the term $s\rho_{\mathrm{g}}$ itself is usually relatively small. α in Eq. (A7) is dependent on τ_{a}, and τ_{a} increases if the absolute value of α is large.

Acknowledgements. The authors are grateful to the Open CLASTER project for allowing us to use the RSTAR package for this research. We would like to thank the AERONET project and its staff for establishing and maintaining the Tamanrasset, Agoufou, Banizoumbou and Saada sites considered in this investigation. We would also like to thank the SKYNET project and its staff for establishing and maintaining the Dunhuang site. Finally, we appreciate the valuable discussions and support provided by Ben Johnson, Satoru Fukuda, Yosuke Sato, Eiji Oikawa, Makiko Hashimoto, Yasushi Mitomi and Matthew Collins. One of the authors was supported by projects by JAXA/EarthCARE and GCOM/C, MEXT/VL for Climate System Diagnostics, MOE/Global Environment Research Fund A-1101, NIES/GOSAT, and MEXT/RECCA/SALSA.

Edited by: Y. Balkanski

References

Ackerman, S. A., Strabala, K. I., Menzel, W. P., Frey, R. A., Moeller, C. C. and Gumley, L. E.: Discriminating clear sky from clouds with MODIS, J. Geophys. Res., 103, 32141–32157, 1998.

Amante, C. and Eakins, B. W.: ETOPO1 1 Arc-Minute Global Relief Model: Procedures, Data Sources and Analysis, NOAA Technical Memorandum NESDIS NGDC-24, 19 pp., March 2009.

Andreae, M. O.: World Survey of Climatology, in: Future Climates of the World, edited by: Henderson-Sellers, A., Elsevier, Amsterdam, Vol. 16, 1995.

Bond, T. C., Doherty, S. J., Fahey, D. W., Forster, P. M., Berntsen, T., DeAngelo, B. J., Flanner, M. G., Ghan, S., Kärcher, B., Koch, D., Kinne, S., Kondo, Y., Quinn, P. K., Sarofim, M. C., Schultz, M. G., Schulz, M., Venkataraman, C., Zhang, H., Zhang, S., Bellouin, N., Guttikunda, S. K., Hopke, P. K., Jacobson, M. Z., Kaiser, J. W., Klimont, Z., Lohmann, U., Schwarz, J. P., Shindell, D., Storelvmo, T., Warren, S. G., and Zender, C. S.: Bounding the role of black carbon in the climate system: A scientific assessment, J. Geophys. Res. Atmos., 118, 5380–5552, doi:10.1002/jgrd.50171, 2013.

Chandrasekhar, S.: Radiative Transfer, New York, Dover, 393 pp., 1960.

Coakley, J. A. and Chylek, P.: The two stream approximation in radiative transfer including the angle of incident radiation, J. Atmos. Sci., 32, 409–418, 1974.

Dubovik, O. and King, M. D.: A flexible inversion algorithm for retrieval of aerosol optical properties from Sun and sky radiance measurements, J. Geophys. Res., 105, 20673–20696, 2000.

Dubovik, O., Holben, B. N., Eck, T. F., Smirnov, A., Kaufman, Y. J., King, M. D., Tanré, D., and Slutsker, I.: Variability of absorption and optical properties of key aerosol types observed in worldwide locations, J. Atmos. Sci, 59, 590–608, 2002.

Dubovik, O., Sinyuk, A., Lapyonok, T., Holben, B. N., Mishchenko, M., Yang, P., Eck, T. F., Volten, H., Munoz, O., Veihelmann, B., van der Zander, Sorokin, M., and Slutsker, I.: Application of light scattering by spheroids for accounting for particle non-sphericity in remote sensing of desert dust, J. Geophys. Res., 111, D11208, doi:10.1029/2005JD006619, 2006.

Food and Agriculture Organization: Digitized Soil Map of the World, World Soil Resources Report 67, FAO, Rome, 1991.

Forster, P., Ramaswamy, V., Artaxo, P., Berntsen, T., Betts, R., Fahey, D. W., Haywood, J., Lean, J., Lowe, D. C., Myhre, G., Nganga, J., Prinn, R., Raga, G., Schulz, M., and Van Dorland, R.: Changes in atmospheric constituents and in radiative forcing, in: Climate Change 2007: The Physical Science Basis, Contribution of Working Group I to the Fourth Assessment Report of the Intergovernmental Panel on Climate Change, edited by: Solomon, S., Qin, D., Chen, Z., Manning, M., Marquis, M., Averyt, K. B., Tignor, M., and Miller, H. L., Cambridge University Press, Cambridge, UK and New York, NY, USA, 129–234, 2007.

Hansen, J., Sato, M., and Ruedy, R.: Radiative forcing and climate response, J. Geophys. Res., 102, 6831–6864, 1997.

Hashimoto, M., Nakajima, T., Dubovik, O., Campanelli, M., Che, H., Khatri, P., Takamura, T., and Pandithurai, G.: Development of a new data-processing method for SKYNET sky radiometer observations, Atmos. Meas. Tech., 5, 2723–2737, doi:10.5194/amt-5-2723-2012, 2012.

Haywood, J. M. and Shine, K. P.: The effect of anthropogenic sulfate and soot aerosol on the clear sky planetary radiation budget, Geophys. Res. Lett., 22, 603–606, 1995.

Haywood, J. M., Francis, P., Osborne, S., Glew, M., Loeb, N., Highwood, E., Tanre, D., Myhre, G., Formenti, P., and Hirst, E.: Radiative properties and direct radiative effect of Saharan dust measured by the C-130 aircraft during SHADE: 1. Solar spectrum, J. Geophys. Res., 108, 8577, doi:10.1029/2002JD002687, 2003.

Haywood, J. M., Pelon, J., Formenti, P., Bharmal, N., Brooks, M., Capes, G., Chazette, P., Chou, C., Christopher, S., Coe, H., Cuesta, J., Dermian, Y., Desboeufs, K., Greed, G., Harrison, M. A. J., Heese, B., Highwood, E. J., Johnson, B. T., Mallet, M., Marticorena, B., Marsham, J., Milton, S. F., Myhre, G., Osborne, S. R., Parker, D. J., Rajot, J-L., Schulz, M., Slingo, A., Tanré, D., and Tulet, P.: Overview of the Dust and Biomassburning Experiment and AfricanMultidisciplinary Monsoon Analysis Special Observing Period-0, J. Geophys. Res., 113, D00C17, doi:10.1029/2008JD010077, 2008.

Haywood, J. M., Johnson, B. T., Osborne, S. R., Baran, A. J., Brooks, M., Milton, S. F., Mulcahy, J, Walters, D., Allan, R. P., Klaver, A., Formenti, P., Brindley, H. E., Christopher, S., and Gupta, P.: Motivation, rationale and key results from the GERBILS Saharan dust measurement campaign, Q. J. Roy. Meteorol. Soc., 137, 1106–1116, doi:10.1002/qj.797, 2011.

Heintzenberg, J.: The SAMUM-1 experiment over southern Morocco: Overview and introduction, Tellus, 61B, 2–11, 2009.

Herman, J. R., Bhartia, P. K., Torres, O., Hsu, C., Seftor, C., and Celarier, E.: Global Distribution of UV-absorbing Aerosols from Nimbus 7/TOMS data, J. Geophys. Res., 102, 16911–16922, 1997.

Holben, B. N., Eck, T. F., Slutsker, I., Tanr'e, D., Buis, J. P., Setzer, A., Vermote, E., Reagan, J. A., Kaufman, Y., Nakajima, T., Lavenu, F., Jankowiak, I., and Smirnov, A.: A federated instrument network and data archive for aerosol characterization, Remote Sens. Environ., 66, 1–16, 1998.

Hsu, N. C., Tsay, S.-C., King, M. D., and Herman, J. R.: Aerosol properties over bright-reflecting source regions, IEEE T. Geosci. Remote Sens., 42, 557–569, 2004.

Huang, J., Minnis, P., Chen, B., Huang, Z., Liu, Z., Zhao, Q., Yi, Y., and Ayers, J. K.: Long-range transport and vertical structure of Asian dust from CALIPSO and surface measurements during PACDEX, J. Geophys. Res., 113, D23212, doi:10.1029/2008JD010620, 2008.

Johnson, B. T. and Osborne, S. R.: Physical and optical properties of mineral dust aerosol measured by aircraft during the GERBILS campaign, Q. J. Roy. Meteorol. Soc., 137, 1117–1130, doi:10.1002/qj.777, 2011.

Kang, J.-Y., Yoon, S.-C., Shao, Y., and Kim, S.-W.: Comparison of vertical dust flux by implementing three dust emission schemes in WRF/Chem, J. Geophys. Res., 116, D09202, doi:10.1029/2010JD014649, 2011.

Kaufman, Y. J.: Satellite sensing of aerosol absorption, J. Geophys. Res., 92, 4307–4317, 1987.

Kaufman, Y. J., Tanr'e, D., Dubovik, O., Karnieli, A., and Remer, L. A.: Absorption of sunlight by dust as inferred from satellite and ground-based remote sensing, Geophys. Res. Lett., 28, 1479–1482, 2001.

Kim, D.-H., Sohn, B.-J., Nakajima, T., Takamura, T., Takemura, T., Choi, B.-C., and Yoon, S.-C.: Aerosol optical properties over East Asia determined from ground-based sky radiation measurement, J. Geophys. Res., 109, D02209, doi:10.1029/2003JD003387, 2004.

Kim, D.-H., Sohn, B.-J., Nakajima, T., and Takamura, T.: Aerosol radiative forcing over East Asia determined from ground-based solar radiation measurements, J. Geophys. Res., 110, D10S22, doi:10.1029/2004JD004678, 2005.

McConnell C. L., Highwood E. J., Coe H., Formenti P., Anderson B., Osborne S. R., Nava S., Desboeufs K., Chen G., and Harrison M. A. J.: Seasonal variations of the physical and optical characteristics of Saharan dust: Results from the Dust Outflow and Deposition to the Ocean (DODO) experiment, J. Geophys. Res., 113, D14S05, doi:10.1029/2007JD009606, 2008.

Meador, W. E. and Weaver, W. R.: Two-stream approximations to radiative transfer in planetary atmospheres: A unified description of existing methods and a new improvement, J. Atmos. Sci., 37, 630–643, 1980.

Mikami, M., Shi, G. Y., Uno, I., Yabuki, S., Iwasaka, Y., Yasui, M., Aoki, T., Tanaka, T. Y., Kurosaki, Y., Masuda, K., Uchiyama, A., Matsuki, A., Sakai, T., Takemi, T., Nakawo, M., Seino, N., Ishizuka, M., Satake, S., Fujita, K., Hara, Y., Kai, K., Kanayama, S., Hayashi, M. , Du, M., Kanai, Y., Yamada, Y., Zhang, X. Y., Shen, Z., Zhou, H., Abe, O., Nagai, T., Tsutsumi, Y., Chiba, M., and Suzuki, J.: Aeolian dust experiment on climate impact: an overview of Japan-China Joint Project ADEC, Global Planet. Change, 52, 142–172, doi:10.1016/j.gloplacha.2006.03.001, 2006.

Mukai, M., Nakajima, T., and Takemura, T.: A study of long-term trends in mineral dust aerosol distributions in Asia using a general circulation model, J. Geophys. Res., 109, D19204, doi:10.1029/2003JD004270, 2004.

Müller, D., Weinzierl, B., Petzold, A., Kandler, K., Ansmann, A., Müller, T., Tesche, M., Freudenthaler, V., Esselborn, M., Heese, B., Althausen, D., Schladitz, A., Otto, S., and Knippertz, P.: Mineral dust observed with AERONET Sun photometer, Raman lidar, and in situ instruments during SAMUM 2006: Shape-independent particle properties, J. Geophys. Res.-Atmos., 115, D07202, doi:10.1029/2009JD012520, 2010.

Müller, D., Lee, K.-H., Gasteiger, J., Tesche, M., Weinzierl, B., Kandler, K., Müller, T., Toledano, C., Otto, S., Althausen, D., and Ansmann, A.: Comparison of optical and microphysical properties of pure Saharan mineral dust observed with AERONET Sun photometer, Raman lidar, and in situ instruments during SAMUM 2006, J. Geophys. Res.-Atmos., 117, D07211, doi:10.1029/2011JD016825, 2012.

Nakajima, T. and Tanaka, M.: Matrix formulation for the transfer of solar radiation in a plane-parallel scattering atmosphere, J. Quant. Spectrosc. Ra. Transfer., 35, 13–21, 1986.

Nakajima, T. and Tanaka, M.: Algorithms for radiative intensity calculations in moderately thick atmospheres using a truncation approximation, J. Quant. Spectrosc. Ra. Transfer., 40, 51–69, 1988.

Nakajima, T., Tanaka, M., Yamano, M., Shiobara, M., Arao, K., and Nakanishi, Y.: Aerosol optical characteristics in the yellow sand events observed in May, 1982 in Nagasaki – Part II Model, J. Meteor. Soc. Japan, 67, 279–291, 1989.

O'Neill, N. T., Eck, T. F., Smirnov, A., Holben, B. N., and Thulasiraman, S.: Spectral discrimination of coarse and fine mode optical depth, J. Geophys. Res., 108, 4559–4573, doi:10.1029/2002JD002975, 2003.

Osborne, S. R., Johnson, B. T., Haywood, J. M., Baran, A. J., Harrison, M. A. J., and McConnell, C. L.: Physical and optical properties of mineral dust aerosol during the Dust and Biomass-burning Experiment, J. Geophys. Res., 113, D00C03, doi:10.1029/2007JD009551, 2008.

Pollack, J. B. and Cuzzi, J. N.: Scattering by non-spherical particles of size comparable to a wavelength: A new semi-empirical theory and its application to tropospheric aerosols, J. Atmos. Sci., 37, 868–881, 1980.

Remer, L. A. and Kaufman, Y. J.: Dynamic aerosol model: Urban/industrial aerosol, J. Geophys. Res., 103, 13859–13871, 1998.

Ryder, C. L., Highwood, E. J., Rosenberg, P. D., Trembath, J., Brooke, J. K., Bart, M., Dean, A., Crosier, J., Dorsey, J., Brindley, H., Banks, J., Marsham, J. H., McQuaid, J. B., Sodemann, H., and Washington, R.: Optical properties of Saharan dust aerosol and contribution from the coarse mode as measured during the Fennec 2011 aircraft campaign, Atmos. Chem. Phys., 13, 303–325, doi:10.5194/acp-13-303-2013, 2013.

Shettle, E. P. and Fenn, R. W.: Models for the aerosol lower atmosphere and the effects of humidity variations on their optical properties, Rep. Tr-79-0214, U.S. Air Force Geophysics Laboratory, Hanscom Air Force Base, Massachusetts, 1979.

Sohn, B.-J., Nakajima, T., Chun, H.-W., and Aoki, K.: More absorbing dust aerosol inferred from sky radiometer measurements at Anmyeon, Korea, J. Meteor. Soc. Japan, 85, 815–823, 2007.

Sokolik, I. N., Winker, D. M., Bergametti, G., Gillette, D. A., Carmichael, G., Kaufman, Y. J., Gomes, L., Schuetz, L., and Penner, J. E.: Introduction to special section: Outstanding problems in quantifying the radiative impacts of mineral dust, J. Geophys. Res., 106, 18015–18027, 2001.

Stamnes, K., Tsay, S. C., Wiscombe, W., and Jayaweera, K.: Numerically stable algorithm for discrete-ordinate-method radiative transfer in multiple scattering and emitting layered media, Appl. Opt., 27, 2502–2509, 1988.

Takemura, T., Okamoto, H., Maruyama, Y., Numaguti, A. Higurashi, A., and Nakajima, T.: Global three-dimensional simulation of aerosol optical depth distribution of various origins, J. Geophys. Res., 105, 17853–17873, 2000.

Takemura, T., Nakajima, T., Dubovik, O., Holben, B. N., and Kinne, S.: Single scattering albedo and radiative forcing of various aerosol species with a global three-dimensional model, J. Clim., 15, 333–352, 2002a.

Takemura, T., Uno, I., Nakajima, T., Higurashi, A., and Sano, I.: Modeling study of long-range transport of Asian dust and anthropogenic aerosols from East Asia, Geophys. Res. Lett., 29, 2158, doi:10.1029/2002GL016251, 2002b.

Tanré, D., Haywood, J., Pelon, J., Léon, J. F., Chatenet, B., Formenti, P., Francis, P., Goloub, P., Highwood, E. J., and Myhre, G.: Measurement and modeling of the Saharan dust radiative impact: Overview of the Saharan Dust Experiment (SHADE), J. Geophys. Res., 108, 8574, doi:10.1029/2002JD003273, 2003.

Torres, O., Bhartia, P. K., Herman, J. R., Ahmad, Z., and Gleason, J.: Derivation of aerosol properties from satellite measurements of backscattered ultraviolet radiation, Theoretical Basis, J. Geophys. Res., 103, 17099–17110, 1998.

Torres, O., Bhartia, P. K., Herman, J. R., Sinyuk, A., Ginoux, P., and Holben, B.: A long term record of aerosol optical depth from TOMS observations and comparison to AERONET measurements, J. Atmos. Sci., 59, 398–413, 2002.

Torres, O., Tanskanen, A., Veihelman, B., Ahn, C., Braak, R., Bhartia, P. K., Veefkind, P., and Levelt, P.: Aerosols and Surface UV Products from OMI Observations: An Overview, J. Geophys. Res., 112, D24S47, doi:10.1029/2007JD008809, 2007.

Whitby, K. T.: The physical characteristics of sulfur aerosols, Atmos. Environ., 12, 135–159, 1978.

World Meteorological Organization: WMO Report of the Experts Meeting on Aerosols and their Climatic Effects, Rep. WCP-55, World Climate Program, Geneva, 1983.

World Meteorological Organization: Scientific Assessment of Ozone Depletion: 2010, WMO Global Ozone Research and Monitoring Project – Report No. 52, 2011.

Yoshida, M. and Murakami, H.: Dust absorption averaged over the Sahara inferred from moderate resolution imaging spectroradiometer data, Appl. Opt., 47, 1995–2003, 2008.

Zhu, L., Martins, J. V., and Remer, L. A.: Biomass burning aerosol absorption measurements with MODIS using the critical reflectance method, J. Geophys. Res., 116, D07202, doi:10.1029/2010JD015187, 2011.